The Journal of General Physiology

Chloride currents from the transverse tubular system in adult mammalian skeletal muscle fibers

Marino DiFranco, Alvaro Herrera, and Julio L. Vergara

Department of Physiology, University of California, Los Angeles, Geffen School of Medicine, Los Angeles, CA 90095

Chloride fluxes are the main contributors to the resting conductance of mammalian skeletal muscle fibers. ClC-1, the most abundant chloride channel isoform in this preparation, is believed to be responsible for this conductance. However, the actual distribution of ClC-1 channels between the surface and transverse tubular system (TTS) membranes has not been assessed in intact muscle fibers. To investigate this issue, we voltageclamped enzymatically dissociated short fibers using a two-microelectrode configuration and simultaneously recorded chloride currents (I_{Cl}) and di-8-ANEPPS fluorescence signals to assess membrane potential changes in the TTS. Experiments were conducted in conditions that blocked all but the chloride conductance. Fibers were equilibrated with 40 or 70 mM intracellular chloride to enhance the magnitude of inward I_{Cl}, and the specific ClC-1 blocker 9-ACA was used to eliminate these currents whenever necessary. Voltage-dependent di-8-ANEPPS signals and I_{Cl} acquired before (control) and after the addition of 9-ACA were comparatively assessed. Early after the onset of stimulus pulses, di-8-ANEPPS signals under control conditions were smaller than those recorded in the presence of 9-ACA. We defined as attenuation the normalized time-dependent difference between these signals. Attenuation was discovered to be I_{Cl} dependent since its magnitude varied in close correlation with the amplitude and time course of I_{Cl}. While the properties of I_{Cl}, and those of the attenuation seen in optical records, could be simultaneously predicted by model simulations when the chloride permeability (P_{Cl}) at the surface and TTS membranes were approximately equal, the model failed to explain the optical data if P_{Cl} was precluded from the TTS membranes. Since the ratio between the areas of TTS membranes and the sarcolemma is large in mammalian muscle fibers, our results demonstrate that a significant fraction of the experimentally recorded I_{Cl} arises from TTS contributions.

INTRODUCTION

The importance of chloride ion fluxes in determining the resting potential of skeletal muscles fibers has long been established (Hodgkin and Horowicz, 1959, 1960). It is currently accepted that in mammalian muscle, chloride ion movements are mostly associated with the abundant expression of the chloride channel isoform ClC-1 (Bretag, 1987; Pusch and Jentsch, 1994). This idea seems to be confirmed by evidence showing that the normal excitability of adult skeletal fibers, afforded by ClC-1, is impaired by mutations that prevent (or alter) the expression of this channel. For example, muscle fibers lacking ClC-1 are hyperexcitable, usually undergoing involuntary contractions after periods of voluntary activity and leading to muscle stiffness (Pusch, 2002). This condition, called myotonia congenita in humans, has also been identified in naturally occurring mutants of goat and mice (Bryant and Morales-Aguilera, 1971; Adrian and Bryant, 1974; Rudel, 1990).

In contrast with the detailed knowledge of the channel biophysics and molecular biology of ClC-1 (Jentsch et al., 2002), its actual distribution between the surface and the transverse tubule system (TTS) membranes remains controversial. There is conflicting electrophysiological and immunohystochemical evidences suggesting both the possibility that ClC-1 channels may be located in either the surface membrane or the TTS membranes (Palade and Barchi, 1977; Dulhunty, 1979; Gurnett et al., 1995; Papponen et al., 2005; Dutka et al., 2008). This key issue must be resolved to attain a realistic model of the electrical excitability in normal and diseased fibers since this essential knowledge would lead not only toward a better understanding of the physiological properties of mammalian muscle fibers, but also of the pathophysiology of myotonias.

It is obvious that the problem of determining the respective distribution of chloride channels between the two external membrane compartments in intact skeletal muscle fibers cannot be addressed by using only classical electrophysiological approaches since the TTS membranes are not accessible to be directly measured electrically. However, as we have previously demonstrated for the inward rectifier K channel in amphibian muscle fibers (Heiny et al., 1983; Vergara et al., 1983; Ashcroft

---

Correspondence to Julio L. Vergara: jvergara@mednet.ucla.edu

Abbreviations used in this paper: 9-ACA, 9 anthracene carboxylic acid; di-8-ANEPPS pyridinium, 4-[2-[6-(dioctylamino)-2-naphthalenyl]ethenyl]-1-(3-sulfopropyl); TTS, transverse tubular system.

The Rockefeller University Press $30.00
J. Gen. Physiol. Vol. 137 No. 1 21–41
www.jgp.org/cgi/doi/10.1085/jgp.201010496

et al., 1985), potentiometric indicator optical signals provide critical information about the average TTS voltage (Heiny and Vergara, 1982; Heiny et al., 1983; Ashcroft et al., 1985; Kim and Vergara, 1998b; DiFranco et al., 2005), thus allowing for a quantitative assessment of the relative distribution of conductances. Namely, the comparison among experimentally recorded ionic currents, optical transients, and model predictions from the radial cable model of the TTS (Adrian et al., 1969; Adrian and Peachey, 1973; Ashcroft et al., 1985; DiFranco et al., 2008) constitutes a dependable method to ascertain the precise contributions from ion channels at the surface and TTS to the total ionic current.

A critical goal of the present work is to define experimentally what membrane distribution of ClC-1 channel is compatible with the experimental data. To this end, we needed to carefully characterize the properties of chloride currents (I_{Cl}) in mammalian fibers under controlled conditions, and then analyze comparatively the features of di-8-ANEPPS (pyridinium, 4-[2-[6-(dioctylamino)-2-naphthalenyl]ethenyl]-1-(3-sulfopropyl)) potentiometric signals recorded in the presence and absence of I_{Cl}. Ultimately, model simulations permitted us to conclude that the only possible arrangement compatible with the overall data is that an approximately equal density of open ClC-1 channel chloride permeability is present in both the surface and TTS membrane compartments. A preliminary account of this conclusion was published previously (Herrera et al., 2010).

MATERIALS AND METHODS

Biological preparation and fiber selection

Animals were handled according to the guidelines laid out by the UCLA Animal Care Committee. Flexor digitorum brevis and interossei muscles from 14–15-wk-old C57BL mice were used. Fibers were enzymatically dissociated as previously described (Woods et al., 2004). The diameter and length of the fibers were 51 ± 2 and 430 ± 15 µm, respectively; the calculated surface area (assuming cylindrical shape) was $7 \times 10^{-4} \pm 4 \times 10^{-5}$ cm^2 ($n = 21$).

Solutions

The compositions of external and internal solutions (in mM) were: TEA-external ($[Cl]_o = 156$), 150 HCl, 10 MOPS, 10 CsOH, 2 $CaCl_2$, 1 $MgCl_2$, 2.10^{-4} TTX, 2.10^{-5} verapamil, pH 7.2 with TEA-OH; internal $[Cl]_I = 1$, 10 HCl, 70 EGTA, 70 MOPS, 5 Na_2-phospho-creatine, 5 Mg-ATP, pH 7.2 with CsOH; internal $[Cl]_I = 40$, 40 HCl, 55 EGTA, 55 MOPS, 5 Mg-ATP, 5 Na_2-phospho-creatine, pH 7.2 with CsOH; internal $[Cl]_I = 70$, 70 HCL, 40 EGTA, 40 MOPS, 5 Mg-ATP, 5-Na_2-phospho-creatine, pH 7.2 with CsOH. The osmolarity of all solutions was 300 ± 5 mOsm/kg H_2O.

Stock solutions were prepared for 9 anthracene carboxylic acid (9-ACA, 1 M in DMSO), verapamil (20 mM in ethanol), and TTX (1 mM in H_2O). Control experiments showed no detectable effects of DMSO or ethanol at the concentrations used. Solid aliquots (29 µg) of di-8-ANEPPS (Invitrogen) were prepared in house by drying appropriate volumes of di-8-ANEPPS dissolved in ethanol in individual eppendorf tubes. Samples were kept at −20°C until used. Di-8-ANEPPS solutions (5 µM) were prepared fresh for every experiment. To this end, the dye was dissolved in 2 µl of pluronic (10% wt/vol in DMSO). This mixture was added to 10 ml of warm Tyrode and sonicated. Unless otherwise indicated, all the chemicals were from Sigma-Aldrich.

Optical arrangement

Dissociated fibers were plated on 3.5-mm coverslip-bottomed Petri dishes placed on the stage of an inverted microscope (Olympus IX-71) equipped with a standard epifluorescence attachment. Bright field and fluorescence images of di-8-ANEPPS–stained fibers were acquired using a CCD camera. Low (bright field) and high magnification images (fluorescence) were obtained with 10x and 100x (1.3 NA, oil immersion) objectives (Olympus), respectively. Bright field images were used to measure fiber dimensions, and fluorescence images were used to evaluate the quality of the TTS staining. Only fibers displaying a sharp sarcomere-banded pattern when viewed under bright-field illumination, and the distinctive double row pattern of di-8-ANEPPS fluorescence bands, which is typical of TTS staining (DiFranco et al., 2005, 2007, 2009) when viewed using epifluorescence illumination, were use for the experiments.

Electrophysiology

A two-microelectrode amplifier (TEV-200A, Dagan Corporation) was used to voltage clamp the fibers and to record chloride currents (I_{Cl}). Two identical electrodes filled with internal solution were used; their resistance was between 8 and 12 MΩ. The resistances of paired electrodes filled with internal solution containing either 40 or 70 mM Cl were not significantly different from each other (9.11 ± 1.65 MΩ and 9.0 ± 1.45 MΩ, respectively; $n = 10$).

Muscle fibers were first impaled under current-clamp conditions. After a period of ∼20 min, which allowed for the equilibration of the pipette solution and the myoplasm (Woods et al., 2004), they were voltage clamped at a holding potential (V_H) equal to the chloride equilibrium potential (V_{Cl}). The absolute values of the outward holding currents were 2–5, 4–8, and 7–10 nA for experiments in which the internal chloride concentration ($[Cl]_i$) was 70, 40, and 10 mM, respectively. Fibers requiring larger currents were rejected. All experiments were performed at room temperature (20–23°C).

Current measurements

Cationic conductances were blocked as follows: (sodium), by adding TTX and replacing Na^+ with TEA in the external solutions; (potassium), by replacing K^+ in the external and internal solutions with TEA and Cs^+, respectively; (calcium), by adding verapamil to the external solutions. When necessary, chloride currents were blocked with 9-ACA (0.5 mM, 10 min). In general, current records are presented free of capacitive transients. To this end, the capacitive component of currents recorded from electrically passive fibers at the end of the experiments were fitted with double exponential functions, scaled and subtracted digitally from every current record.

Two stimulation protocols were used to record I_{Cl}: (1) a single-pulse protocol in which rectangular pulses (typically 50–100 ms in duration) of both polarities were applied from V_H and; (2) a three-pulse protocol consisting of a conditioning pulse (P1) and two consecutive test pulses (P2 and P3). During P1, the cell was depolarized to +60 mV for 150 ms, thus allowing for maximal activation of I_{Cl} (Fahlke and Rudel, 1995; Lueck et al., 2007). P2 was of variable amplitude (typically from −140 to 140 mV, in 20-mV increments) and constant duration (200 ms). Tail currents during P2 were used to determine the voltage dependence of the current through the open channels. P3 had constant amplitude (typically to −100 mV) and duration (50 ms). The normalized amplitudes of the tail currents at the onset of P3 were used to determine the voltage dependence of the relative open probability of the chloride channels (Pusch et al., 2000; Bennetts et al., 2007; Lueck et al., 2007).

Throughout this paper, ionic currents are expressed in units of µA/cm^2; however, to allow for comparisons with data from other laboratories, its equivalence in A/F can be readily calculated. To this end, membrane capacitances were calculated from the integral of the linear capacitive components of currents recorded during small voltage pulses when the fibers were bathed in solutions blocking all ionic conductances (DiFranco et al., 2008). The average measured values of membrane capacitance per unit surface membrane were 5.2 ± 0.3 µF/cm^2 ($n = 21$).

Optical recording of di-8-ANEPPS signals

Membrane potential changes in the TTS were measured using the fluorescent potentiometric indicator di-8-ANEPPS as previously described (DiFranco et al., 2005). In brief, fibers were stained for 30 min in Tyrode containing 5 µM di-8-ANEPPS. Afterward, the fibers were washed in plain Tyrode. The light source for fluorescence detection was a tungsten-halogen lamp driven by a stabilized power supply. Illumination was controlled with an electromagnetic shutter (Uniblitz) under computer command. Di-8-ANEPPS fluorescence was selected using a fluorescence cube with an excitation filter of 530 ± 15 nm, a 550-nm dichroic mirror, and a 600-nm long pass filter. The illumination spot on the muscle fiber was adjusted to form a disc of ~25 µm in diameter, which was focused (using a 100x, 1.4 NA objective) at the geometrical center of the x, y, and z axes of the fiber. The illumination spot circumscribed the area of the fiber where the voltage microelectrode was impaled. Di-8-ANEPPS fluorescence signals were single sweeps of fluorescence changes, as detected with a photodiode (UV-001, OSI Optoelectronics) connected to a patch-clamp amplifier (Axopatch 2A, Molecular Devices). Optical signals are expressed here in terms of ΔF/F, defined as the change of fluorescence (ΔF) divided by the resting fluorescence (F) (Vergara et al., 1978; DiFranco et al., 2005, 2008).

Characterization of di-8-ANEPPS signals recorded under passive conditions

The deconvolution of di-8-ANEPPS fluorescence changes, in terms of the voltage changes at the TTS that they report, has been traditionally performed using a linear regression calibration of the steady-state fluorescence levels (in ΔF/F) versus the amplitude of voltage-clamp steps from V_H (in mV) in fibers rendered electrically passive (Kim and Vergara, 1998a, b; DiFranco et al., 2005, 2008). Since in this paper we will present data correlating the effects of I_{Cl} on the properties of di-8-ANEPPS signals in fibers voltage clamped at different V_Hs while equilibrated in 10, 40, and 70 mM $[Cl]_i$, we were required to characterize the properties of these signals at passive conditions. Fig. 1 A shows a family of fluorescence transients, recorded from a passive fiber equilibrated with 40 mM $[Cl]_i$ and clamped at −40 mV, in response to voltage steps (not shown) ranging from −120 to 120 mV every 20 mV. As previously reported (DiFranco et al., 2005), under the illumination conditions of the current experiments (see above), depolarizing pulses result in negative di-8-ANEPPS fluorescence transients (red traces), while hyperpolarizations produce positive ΔF/F changes (black traces). It should be noticed that, though the voltage transition imposed at the fibers occurs within ~50 µs in our two microelectrode system, because di-8-ANEPPS transients arise mostly from the TTS (DiFranco et al., 2005; Woods et al., 2005), their rising and falling phases display much slower transitions with on and off τs of 0.38 ± 0.05 and 0.33 ± 0.034 ms ($n = 5$), respectively. It should be also noticed that, in this fiber, transients elicited by hyperpolarizing pulses are larger than those elicited by depolarizing pulses of the same amplitude. This is also appreciated in Fig. 1 B, which plots the steady-state amplitude of ΔF/F transients as a function of the pulse amplitude; when the dye responses are fitted to linear regressions, the slope is larger for hyperpolarizing pulses (−19.2%/100 mV) than for depolarizing

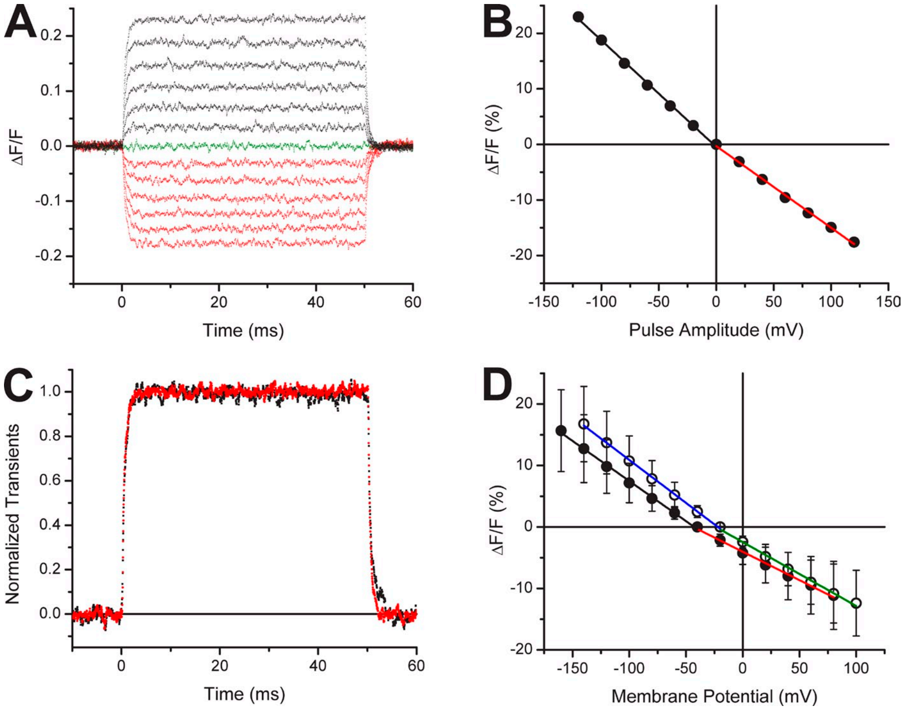

Figure 1. Calibration of di-8-ANEPPS transients in passive fibers. (A) Di-8-ANEPPS transients (single sweeps) acquired in response to depolarizing (red traces) and hyperpolarizing voltage-clamp pulses (black traces) applied from V_H = −40 mV. Pulse amplitude was varied from −120 to 120 mV in 20-mV increments. The green trace shows the baseline noise (0 mV pulse). Fiber parameters: radius = 22 µm; length = 348 µm; capacitance: 6.6 µF/cm^2. (B) Steady-state amplitude of di-8-ANEPPS transients plotted as a function of the pulse amplitude. The linear regression fits to the data for hyperpolarizing and depolarizing pulses are shown as solid black and red lines, respectively. (C) Superposition of transients elicited by −120-mV (red trace) and +120-mV pulses (black trace). Both traces were normalized, and the trace in response to the −120-mV pulse was inverted. (D) Voltage dependence of the amplitude of di-8-ANEPPS transients recorded from fibers clamped at −40 mV (solid symbols, $n = 4$) and −20 mV (open symbols, $n = 8$). The slopes of the linear regressions through the solid symbols (in %/100 mV) are (mean ± SD): −13.1 ± 2.8 (black line) and −9.3 ± 2.3 (red line), for hyperpolarizing and depolarizing pulses, respectively. The slopes of the linear regressions through the open symbols are: −14.0 ± 1.7%/100mV (blue line) and −10.7 ± 1.5%/100mV (green line), for hyperpolarizing and depolarizing pulses, respectively. All data included in this figure were obtained at the end of experiments after rendering the fibers electrically passive by blocking all activatable conductances.

pulses (−14.7%/100 mV). Interestingly, Fig. 1 C shows that when ΔF/F transients elicited by −120 mV (red trace) and +120 mV (black trace) pulses are scaled and superimposed, regardless of the difference in amplitude, the rising and falling phases of both transients have almost identical kinetic properties.

The average amplitude of di-8-ANEPPS transients (ΔF/F %) recorded from fibers equilibrated with 40 and 70 mM $[Cl]_i$ (V_H = −40 and −20 mV, respectively) are plotted versus the membrane potential in Fig. 1 D. A comparative analysis of the linear regressions (solid lines) shown in Fig. 1 D demonstrates that their slopes are significantly steeper for data obtained in response to hyperpolarizing, with respect to that obtained with depolarizing pulses (paired *t* test, $P < 0.05$); however, they are not different for pulses of the same polarity obtained at either 40 or 70 mM $[Cl]_i$ ($P > 0.5$; see Fig. 1 D, legend). Regardless of the mechanistic reasons why di-8-ANEPPS signals display slightly different amplitudes in response to positive and negative voltage pulses of the same magnitude in fibers under passive conditions, the constancy of their kinetic properties for all pulses (as shown in Fig. 1 C), and the possibility to obtain accurate regression slopes at the end of each experiment (Fig. 1 D), validate the deconvolution of the transients in terms of the changes in membrane potential in the TTS that they are reporting.

Model simulations

The radial cable model is described in the Appendix.

Data acquisition and statistical analysis

Voltage, current, and fluorescence records were filtered at 10, 1, and 2 kHz, respectively, using multiple pole analogue Bessel filters. Data points were sampled every 30 µs, using a data acquisition interface (PCI-6221, National Instruments) and custom software written in LabView (National Instruments). Unless otherwise stated, pooled data are expressed as mean ± SEM. Significance was set $P < 0.05$.

RESULTS

Currents recorded in high internal and external chloride concentrations in response single-pulse stimulation

For simplicity, we wanted to establish the possibility to record robust chloride currents using a single-pulse protocol. To this end, isolated muscle fibers were equilibrated with 40 or 70 mM internal $[Cl]_I$, and voltage clamped at V_H = −40 or −20 mV, respectively. Fig. 2 A shows that outward currents detected in response to positive voltage-clamp pulses are almost time independent, whereas inward currents elicited by negative pulses display the characteristic transient behavior with an early peak (I-peak) followed by a strong deactivation toward a steady-state value (I-ss). It is apparent in this figure that the deactivation of the currents is faster and more pronounced the larger the hyperpolarization (Fahlke and Rudel, 1995; Lueck et al., 2007). As clearly demonstrated in Fig. 2 B, the great majority (>95%) of the inward currents recorded under these conditions is blocked by 9-ACA, leaving a current component that is mostly time independent. The kinetic properties, voltage dependence, and sensitivity to 9-ACA shown in the current records of Fig. 2 (A and B) are hallmarks of the currents carried through the skeletal muscle ClC-1 chloride channel (Bretag, 1987; Fahlke, 2001). As expected, the 9-ACA–sensitive currents (I_{Cl}), calculated as the difference between the currents recorded before and during 9-ACA application (Fig. 2 C), are remarkably similar to the total ionic currents shown in Fig. 2 A. Thus, the peak and steady-state components of the 9-ACA–sensitive components (I_{Cl}-peak and I_{Cl}-ss, respectively) differ slightly from those of the total ionic current records. This is better illustrated in I-V plots (Fig. 2 D) of I_{Cl}-peak (black symbols), I_{Cl}-ss (red symbols), and (time independent) 9-ACA–insensitive residual currents (blue symbols). It can be observed that the 9-ACA–insensitive currents do not amount for too much with respect to I_{Cl}-peak and I_{Cl}-ss, except at relatively large depolarizations. Interestingly, Fig. 2 D shows that while I_{Cl}-peak displays strong inward rectification, I_{Cl}-ss displays an inverted bell-shape distribution with a minimum at approximately −85 mV, which arises from the crossover of the tail currents, resulting from acceleration of the deactivation at larger hyperpolarizing pulses. As indicated before, these general features of 9-ACA–sensitive currents are reminiscent of those previously ascribed to ClC-1 channels (Bretag, 1987; Fahlke, 2001).

The presence or absence of inward currents did not have significant effects on the membrane potential recorded by the voltage microelectrode, as illustrated in the insets of Fig. 2 (A and B, respectively). Namely, the voltage records display the rectangular shapes of the command voltage steps at every amplitude; also, they were not significantly different when obtained in the absence (Fig. 2 A, inset) or presence of 9-ACA (Fig. 2 B, inset).

Di-8-ANEPPS transients recorded in the presence and absence of chloride currents

Having established that a single-pulse protocol yields large I_{Cl}s, we studied the effects of those currents on the electrical behavior of the TTS. To this end, we simultaneously acquired I_{Cl} and di-8-ANEPPS fluorescence transients in fibers equilibrated with high $[Cl]_i$. Fig. 3 (A and B) shows transients recorded before and during exposure to 9-ACA, respectively, in a fiber internally equilibrated with 40 mM $[Cl]_i$. It should be noted that the optical traces in Fig. 3 (A and B) were inverted (and expressed as negative ΔF/F values) to graphically match the convention that positive and negative voltage changes are represented as upward and downward deflections, respectively. Unless otherwise noted, this convention will be maintained throughout the rest of the paper.

A direct comparison of the properties of transients obtained with homologous pulses in Fig. 3 (A and B) permits us to observe that there is a clear discrepancy in the early phase of the signals (onset) obtained before and after blocking I_{Cl}, which is particularly notorious for large hyperpolarizing pulses. For example, the cyan trace shown Fig. 3 B (in 9-ACA) shows a robust transition of ∼0.18 ΔF/F at the onset of the pulse to −120 mV, while the corresponding signal obtained under control conditions shows a much reduced jump of ~0.13 ΔF/F for the same pulse. Interestingly, these differences in the signals recorded before and after 9-ACA are progressively less notorious for smaller hyperpolarizations (e.g., red, violet, blue, and purple traces in Fig. 3, A and B). To complete the picture of what might be occurring, we should call the reader's attention to the current traces obtained for each of the pulses in the absence and in the presence of 9-ACA, as presented in Fig. 3 (C and D, respectively). At the onset of the −100-mV pulse, there is a large inward I_{Cl}-peak (~580 µA/cm^2) that is virtually absent in the presence of 9-ACA. Thus, we may hypothesize that I_{Cl}-peak is responsible for the reduction in magnitude of the TTS signal shortly after the pulse onset. In agreement with this view, the smaller I_{Cl}-peaks detected in response to smaller hyperpolarizations (e.g., red, violet, blue, and purple traces in Fig. 3 C) are associated with smaller differences between the early portion of the TTS signals recorded before and after 9-ACA application. Furthermore, for depolarizing pulses, outward currents have less effect on the TTS signals (e.g., compare gray traces in Fig. 3, A and B) because their magnitudes are significantly smaller that those elicited by equal amplitude hyperpolarizing pulses (e.g., compare gray and cyan traces in Fig. 3 C). Perhaps the most persuasive argument in favor of the hypothesis that the differences between TTS signals recorded before and after the application of 9-ACA are current dependent is that at the end of the hyperpolarizing pulses, when the currents have decayed to smaller steady-state values, there are significantly less differences in the TTS signals recorded under both conditions (e.g., note the similarity among the cyan, red, violet, blue, and purple traces at the end of the pulses in Fig. 3, A and B).

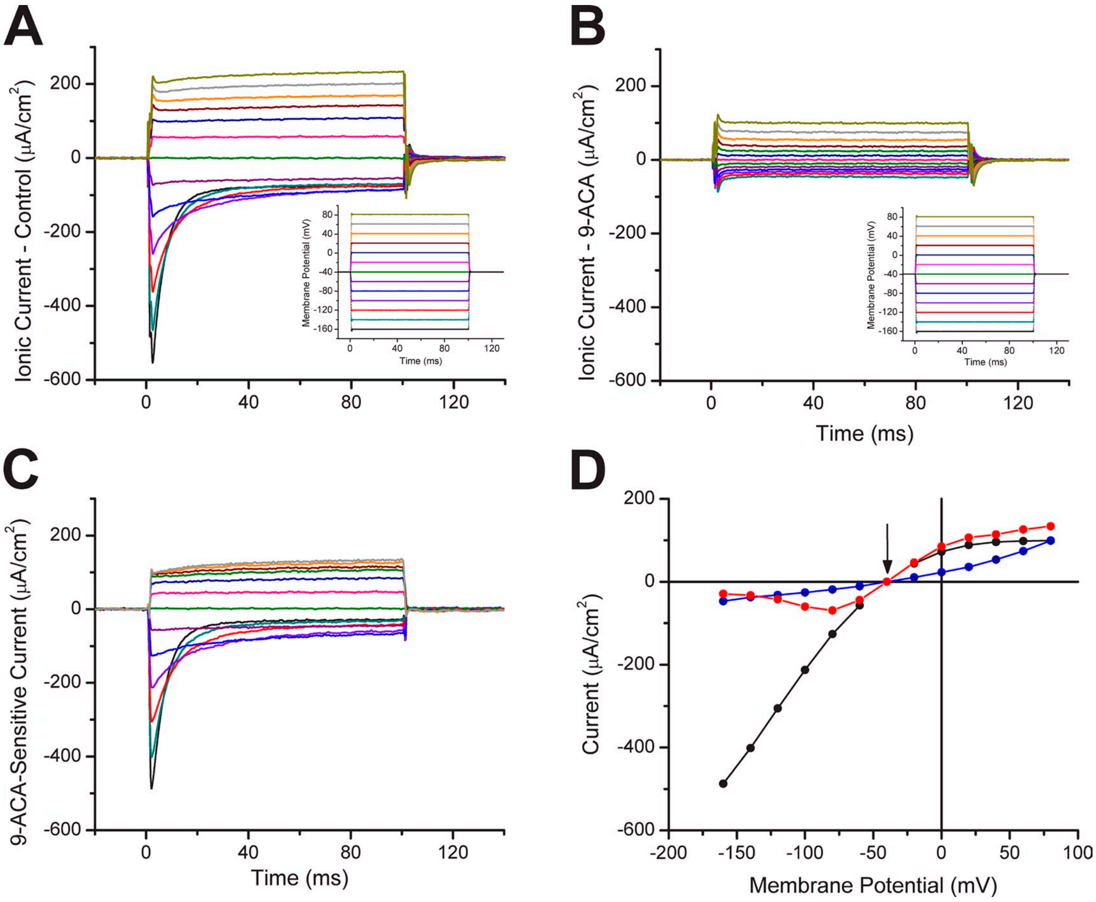

Figure 2. Currents elicited by single pulses in a fiber equilibrated with 40 mM $[Cl]_i$. (A) Total ionic currents recorded in TEA-external. The inset shows the corresponding membrane potential records. (B) Residual currents in the presence of 0.5 mM 9-ACA. The inset shows the corresponding membrane potential records. (C) 9-ACA–sensitive currents obtained by one-to-one subtraction of the records in B from those in A. In A–C, pulses ranged from –120 to +120 mV, applied every 20 mV from a V_H = –40 mV. Trace color sequence: black (–120 mV), cyan, red, violet, blue, purple, olive, pink, dark blue, brown, orange, gray, and dark yellow (120 mV). (D) Voltage dependence of peak and steady-state values of 9-ACA–sensitive currents (I_{Cl}-peak and I_{Cl}-ss, black and red symbols, respectively). The steady-state values of the 9-ACA–insensitive currents are plotted in blue symbols. The arrow indicates V_H. Fiber parameters: radius = 26 µm; length = 364 µm; capacitance: 4.9 µF/cm^2.

Radial cable model simulations predict the features of di-8-ANEPPS signals, provided that a significant fraction of I_{Cl} arises from the TTS

The results described previously demonstrate that the properties of di-8-ANEPPS transients, particularly at the onset of hyperpolarizing pulses, depend crucially on the presence or absence of I_{Cl}. As illustrated previously for the inward rectifier K conductance of amphibian muscle fibers (Heiny et al., 1983; Ashcroft et al., 1985), an accurate way to test the dependence of TTS voltage changes on the presence of an intrinsic conductance is to (a) predict these changes using a radial cable model of the TTS; (b) provide the basis for what the optical signals may represent in terms of TTS voltage changes (Ashcroft et al., 1985; Kim and Vergara, 1998b); and (c) compare the optical data with the model predictions of the optical signals. A detailed description on how steps a and b will be fulfilled in the current work, including a simple model for the ClC-1 capable of predicting the properties of I_{Cl} records, is provided in the Appendix. Fig. 4 illustrates our attempts to explain the results obtained from a fiber internally equilibrated with 70 mM $[Cl]_i$. Fig. 4 A shows the di-8-ANEPPS signals recorded in response to −120, −80, −40, 0, 40, and 80-mV voltage-clamp pulses (100 ms), applied from $V_H = -20$ mV. Fig. 4 D displays the corresponding ionic current records. The most relevant features of these experimental records resemble those previously described for Fig. 3 (A and C). Namely, the relatively large transient inward currents elicited by large negative pulses (e.g., −80 and −100 mV) are associated with early depressions in the di-8-ANEPPS signals, which are less apparent for signals associated with smaller negative pulses (or positive pulses) while the currents are less prominent. To allow for a comparison with model predictions of average TTS voltage changes (see Appendix), the di-8-ANEPPS signals were deconvoluted to transform ΔF/F values into membrane potential by using an intrinsic regression formula (Fig. 4, legend) based on passive data obtained in the same fiber at the end of the experiment. Fig. 4 (B and E) illustrates the results of model predictions (for optical signals and currents, respectively) that incorporated, as a first approximation, an identical density of open channel chloride permeability (in this case, $P_{Cl} = 5.75 \times 10^{-5}$ cm/s) both at the surface and TTS membrane compartments. It is important to note that with the model parameters used (see Fig. 4 legend and Appendix), it is possible to attain remarkably close predictions of the kinetic features and voltage dependence of both the TTS membrane potential changes and currents (Fig. 4, B and E) in comparison with those recorded experimentally (Fig. 4, A and D, respectively). Interestingly, the model concurs with the experimental data in that TTS voltage changes reached steady-state values that are significantly closer to the command voltages than during the onset of the pulses. This is particularly notorious for large hyperpolarizations, when I_{Cl} drastically (and rapidly) deactivates to very small steady-state levels.

The question that remains is, do these favorable comparisons between data and model predictions represent

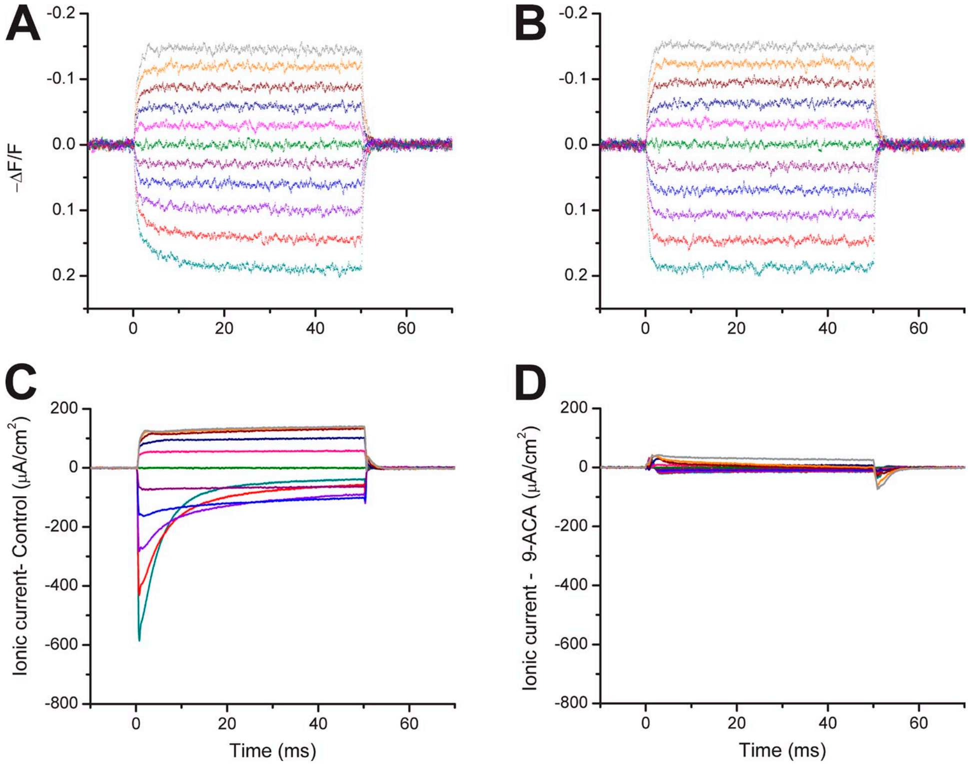

Figure 3. Di-8-ANEPPS transients and currents recorded before and after blocking I_{Cl}. (A) Single sweep di-8-ANEPPS records obtained in a fiber with 40 mM $[Cl]_i$ under control conditions. Pulses (50-ms rectangular steps) ranging in amplitude from −100 to +100 mV were applied every 20 mV from a $V_H = -40$ mV (trace colors: cyan, red, violet, blue, purple, olive, pink, dark blue, brown, orange, and gray, respectively). (B) Di-8-ANEPPS transients recorded in response to the same pulses as in A, but in the presence of 9-ACA. (C) Ionic current records detected simultaneously with the transients in A. (D) Ionic current records detected simultaneously with the transients in B. Same fiber as in Fig. 1 A.

a coincidental result, or are they representative of the general features and membrane distribution of chloride channels, and of their influence on the TTS membrane potential? The rest of the paper will be devoted to answer this question. Meanwhile, Fig. 4 (C and F) illustrates a situation that must be discarded at once; namely, that all the chloride permeability is concentrated in the sarcolemma of the muscle fiber. As it is clearly illustrated in Fig. 4 C, model predictions in this case bluntly fail to reproduce the main features of the di-8-ANEPPS transients shown in Fig. 4 A. It is worth noting that the simulated traces in Fig. 4 C resemble those recorded after blocking I_{Cl} with 9-ACA, as shown in Fig. 3 B, when the fibers are rendered passive by blocking all conductances. However, the simulations presented in Fig. 4 (C and F) include sufficient chloride permeability ($P_{Cl} = 1.37 \times 10^{-4}$ cm/s), albeit only at the surface membrane, to account for the relatively large ionic currents recorded experimentally. It is important to note that, unlike the current simulations shown in Fig. 4 E in which ~60% of the peak inward current arises from TTS membranes (not depicted), the currents predicted in Fig. 4 F arise exclusively from the surface membrane. In fact, the apparently slower kinetic features of the current traces shown in Fig. 4 E, as compared with those in Fig. 4 F, illustrate that the average current contributions from the TTS are affected by the overall distributed nature of the electrical properties of this membrane compartment.

The attenuation observed in TTS signals depends on I_{Cl}

An unavoidable conclusion from the results described above seems to be that there is a direct correlation between the magnitude and kinetics of I_{Cl} with the depressions in the magnitude of di-8-ANEPPS transients elicited, in association with the largest currents, in response to hyperpolarizing pulses. To further test these ideas, and more importantly, to establish a rigorous framework for quantitative analysis, we defined a protocol to measure the I_{Cl}-dependent attenuation observed in optical signals. Fig. 5 illustrates this for a fiber equilibrated with 70 mM $[Cl]_i$. Fig. 5 A shows (superimposed) optical transients recorded in the absence (black trace) and presence (red trace) of 9-ACA. As previously highlighted, the kinetics of these transients differs greatly during the early phase of the pulse; consequently, a time-dependent difference between them is readily observable and will be the basis for our assessment of the

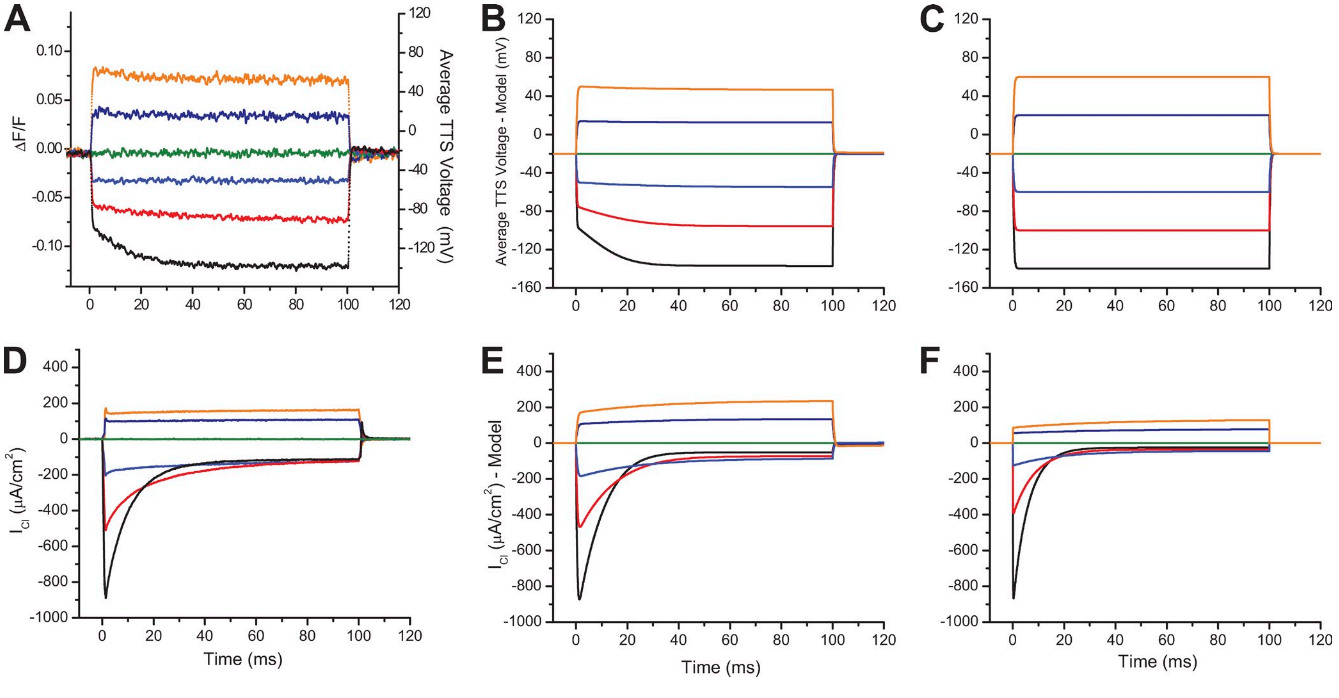

Figure 4. Comparison between single-pulse experimental data and radial cable model predictions. (A) Di-8-ANEPPS transients recorded in response to −120, −80, −40, 0, 40, and 80-mV pulses from $V_H = -20$ mV (black, red, blue, green, dark blue, and orange traces, respectively). The deconvolution of ΔF/F (left vertical axis) into membrane potential (right vertical axis) was done according to the regression formula $V_m = (\Delta F/F - 0.016)/6.93 \times 10^{-4}$ (in mV). (B) Model predictions of the TTS membrane potential assuming equal chloride permeability density in the TTS and surface membranes and the geometrical parameters of the fiber (see below). (C) Model predictions of the TTS membrane potentials assuming that I_{Cl} is located only in the surface membrane. (D) Experimental ionic currents corresponding to the optical records in A. E and F are the predicted ionic currents associated with the simulated traces in B and C, respectively. Fiber parameters: radius = 24 µm; length = 360 µm; capacitance: 6.4 µF/cm².

attenuation. However, to reduce uncertainties due to noise, the experimental traces were not directly subtracted; instead, they were fitted with double exponential functions (Fig. 5 A, red and black solid lines) and then subtracted. We define attenuation (in percentage) as the difference between the before and after 9-ACA line fits (red minus black traces in Fig. 5 B), normalized by the amplitude of the 9-ACA blocked trace (Fig. 5 B, red trace), and multiplied by 100. Attenuation is shown for this particular trial as the green trace in Fig. 5 B. As can be seen, the extent of the attenuation in the optical signals is time dependent, with its peak delayed with respect to the onset of the pulse (see Fig. 5 B). As illustrated in Fig. 5 C, the peak of the attenuation trace (~28%) occurs in closer synchrony, but still a bit later (~2 ms) than the peak of the 9-ACA–sensitive I_{Cl} record (830 μA/cm^2; Fig. 5 C, blue trace). Note that I_{Cl} rises faster and reaches its maximum before the attenuation does (green trace). Furthermore, I_{Cl} decays faster than the attenuation trace. As noted previously, this time shift between current and optical records is a strong indication that the optical signals originate from a membrane compartment that is affected by the magnitude of the current, but in which voltage changes cannot occur instantaneously (i.e., the TTS membranes).

Once we have operationally defined a method to calculate the attenuation from pairs of di-ANEPPS records, we can accurately establish the effects of 9-ACA–sensitive I_{Cl} on the TTS signals, and the voltage dependence of these effects. This is exemplified in Fig. 6 for the same fiber of Fig. 4. Fig. 6 A shows attenuation traces calculated at various voltages from the experimental records in Fig. 4 A and their corresponding records acquired after 9-ACA treatment (not depicted). Fig. 6 B shows the 9-ACA–senstive I_{Cl} records recorded (simultaneously) at the same voltages. It can be seen that the kinetics of the attenuation traces approximately emulates that of the current traces. For example, a large and rapidly decaying inward current (e.g., 780 to 61 μA/cm^2, τ_{decay} ~ 17 ms; Fig. 6 B, black trace), recorded in response to a large hyperpolarizing pulse of −120 mV, yields a large and rapidly decaying attenuation trace (30 to 3%, τ_{decay} ~ 16 ms; Fig. 6 A, black trace). In contrast, smaller and steadier inward currents elicited in response to smaller hyperpolarizations (e.g., 170 μA/cm^2 in response to −40 mV pulse; Fig. 6 B, brown trace), or

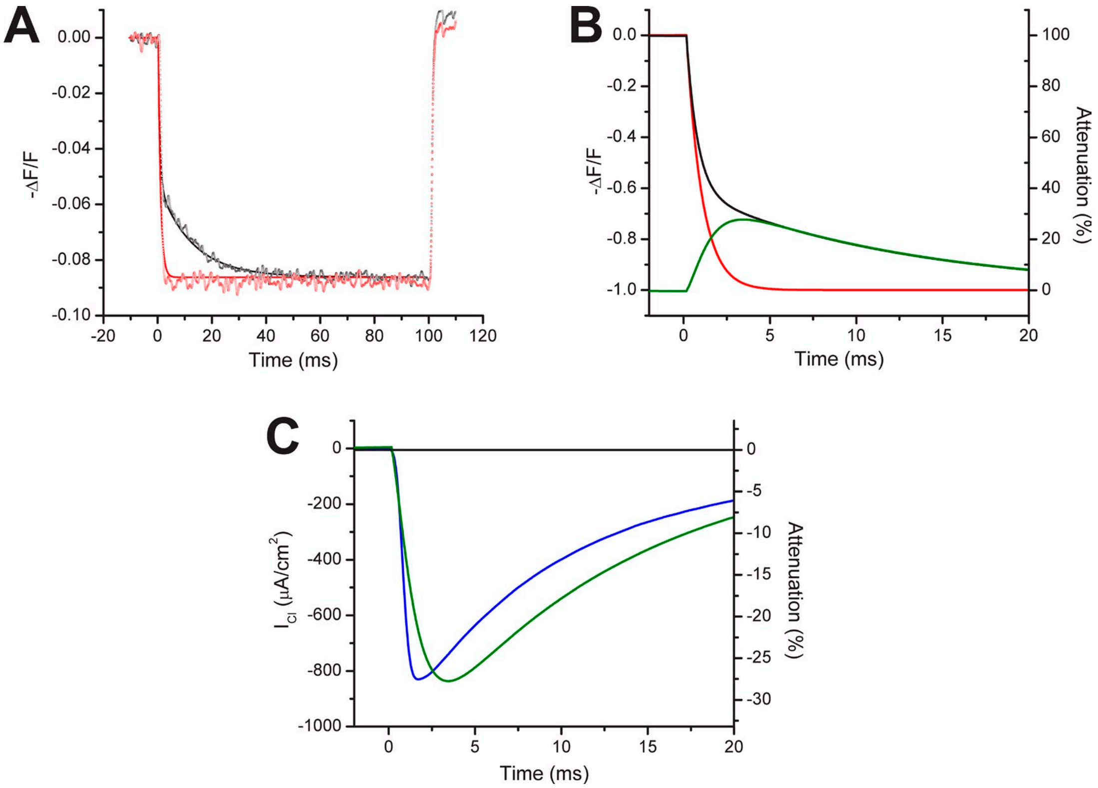

Figure 5. Current-dependent attenuation. (A) Di-8-ANEPPS transients recorded in response to a −120-mV (100-ms) pulse before (black noisy trace) and after blocking I_{Cl} with 9-ACA (red noisy trace). The solid lines are double exponential fits to the corresponding experimental records. The fiber was equilibrated with 70 mM $[Cl]_i$. (B) The black and red lines are the double exponential fits to the di-8-ANEPPS transients normalized to the maximal steady-state value and displayed at an expanded time scale. The current-dependent attenuation of the optical signal (green trace) was calculated by subtraction of these two traces and expressed as percentage change (see text). (C) Superimposed time course of the attenuation trace (green trace) presented inverted to allow for kinetic comparison with the 9-ACA–sensitive I_{Cl} (blue trace).

outward currents in response to depolarizations, result in attenuations that are smaller and have a more constant time course (e.g., ~15%; Fig. 6 A, blue trace). This pattern can be seen more clearly in Fig. 6 C, where we graph peak values of the attenuation records (black bars) and steady-state values (red bars) as a function of the membrane potential. It can be seen that an early attenuation as large as 30% is attained in response to a pulse to −140 mV, but that steady-state attenuation for the same pulse is negligible (~3%). This remarkable disparity between initial and steady-state attenuation most likely reflects the large difference between peak and steady-state I_{Cl} at this voltage, as illustrated in Fig. 6 D. For progressively smaller hyperpolarizations, peak attenuations decrease in size while the peak inward currents do the same. Interestingly, as illustrated in Fig. 6 D, while the peak inward current decreases with smaller hyperpolarizations (black symbols), the steady-state I_{Cl} shows a characteristic increase (red symbols), which is reflected in the appearance of a visible increase in steady-state attenuation in the optical records (Fig. 6 C, red bars). It should be noted that, with the caveat that attenuations are always positive values and not linearly related to the currents, there is an apparent similarity between the bell-shaped voltage dependences seen at the steady state for both I_{Cl} and attenuation. Also, while the optical signals recorded from a region close to the voltage microelectrode (~20 µm) displayed significant current-dependent attenuations, the activation of I_{Cl} had no detectable effects on voltage records from the voltage electrode (unpublished data).

Voltage dependence of the peak attenuation observed in TTS voltage changes in fibers with different $[Cl]_i$

We have already validated the concept that the attenuation observed in di-8-ANEPPS transients is dependent on the magnitude of 9-ACA–dependent I_{Cl} currents using experimental data from individual fibers. We now extend these observations to fiber populations with three different internal chloride concentrations: 70, 40, and 10 mM. Fig. 7 shows pooled data for the voltage dependence of peak attenuations (Fig. 7, A–C) and currents (Fig. 7, D–F) measured at each of these conditions, respectively. As can be seen in Fig. 7 (D–F), average maximal peak inward 9-ACA–sensitive currents were larger the larger the intracellular $[Cl]_i$. For example, for hyperpolarizations to –140 mV, the average values of 9-ACA–dependent I_{Cl} were −672 ± 64 ($n = 8$) and −471 ± 73 µA/cm^2 ($n = 4$) for 70 and 40 mM $[Cl]_i$, respectively. Comparative statistical analysis of the data in Fig. 7 (D–F) demonstrates that, for every hyperpolarization tested, differences in the magnitude of I_{Cl} for every $[Cl]_i$ tested were significant. It is also noticeable in Fig. 7 (D–F) that the reversal potential for the currents moved toward more positive values as $[Cl]_i$ increased, indicating that the reversal potentials are very close to V_{Cl}. This suggests that the myoplasmic $[Cl]_i$ effectively equilibrated with those in the pipette solutions, and that errors

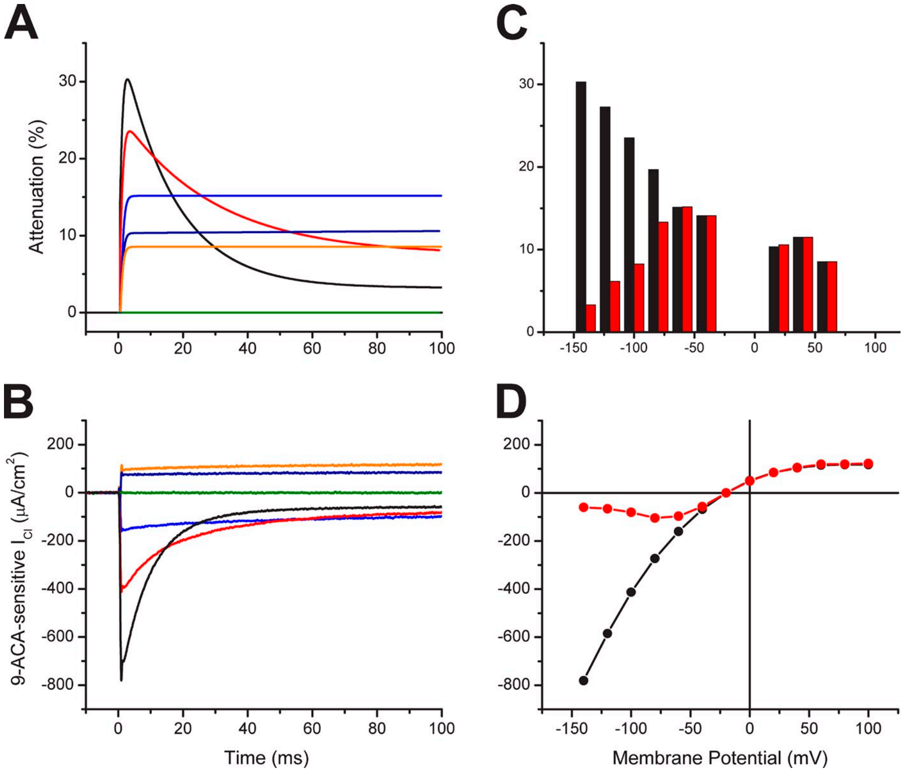

Figure 6. Comparison of attenuations and currents at several voltages. (A) Superimposed attenuation traces calculated from di-8-ANEPPS records before and after 9-ACA application, obtained from the same fiber as in Fig. 4. Black, red, blue, green, dark blue, and orange traces correspond to −120, −80, −40, 0, 40, and 80 mV pulses, respectively. (B) 9-ACA–sensitive I_{Cl} recorded with the same pulses as in A. (C) Bar graphs showing the voltage dependence of the maximal (black bars) and steady-state (red bars) attenuation. Part of the data shown in these graphs was obtained from the traces in A. (D) Voltage dependence of the peak (black symbols) and steady-state (red symbols) values of the 9-ACA–sensitive I_{Cl}. Part of the data shown in these plots was obtained from the records in B.

potentially introduced by differential junction potentials in the pipettes are of minimal import.

The magnitude of the maximal peak attenuations (at −140 mV), calculated from optical data at the three $[\mathrm{Cl}]_\mathrm{I}$, were also statically different from each other. Though there is an apparent correlation between the average peak attenuation data shown in Fig. 7 (A and B) and the magnitude of the currents in Fig. 7 (D and E), this is less notorious than the voltage-to-voltage correlation seen in individual fibers (e.g., Fig. 6 C, black bars). The most likely explanation for this loss of correlation is that there is a substantial fiber-to-fiber variability in the ΔF/F of the optical signals (see Fig. 1 D). Nevertheless, the analysis of the data in Fig. 7 A shows that the peak attenuation is significantly larger at −140 mV for membrane potentials more positive than −100 mV. As shown in Fig. 7 B, the significance of the differences among various voltages is less rigorous for smaller currents. As illustrated in Fig. 7 (C and F), the reduction of the $[\mathrm{Cl}]_\mathrm{i}$ to 10 mM did result in significantly smaller 9-ACA–sensitive currents, which are weakly voltage dependent; maximal values of 70 ± 26 $\mu\mathrm{A/cm}^2$ were recorded with strong (120 mV) depolarizations (Fig. 7 F). Interestingly, the attenuation levels under these $[\mathrm{Cl}]_\mathrm{i}$ conditions (Fig. 7 C) are small (hardly getting above 5%) and difficult to detect, as suggested by the relatively large error bars.

Properties of TTS signals and current records in response to a three-pulse protocol

To obtain further evidence of the effects of the presence of a fraction of the chloride currents in the TTS, we used a three-pulse voltage protocol that has been widely used by other investigators to characterize the properties of ClC-1 currents in a variety of preparations, including skeletal muscle (Rychkov et al., 1996; Zhang et al., 2000; Lueck et al., 2007; Zifarelli and Pusch, 2008). Fig. 8 A shows the time course of di-8-ANEPPS transients recorded from a fiber equilibrated with 70 mM $[\mathrm{Cl}]_\mathrm{i}$ (V_H = −20 mV) in response to a constant P1 (150 ms to +60 mV) followed by variable test pulses (P2, 200 ms) and a fixed P3 (50 ms to −100 mV). It can be observed that transients recorded in response to large hyperpolarizing P2 pulses (i.e., black and red traces) display beautifully the characteristic rounding that reflects the attenuation of the TTS voltage changes due to

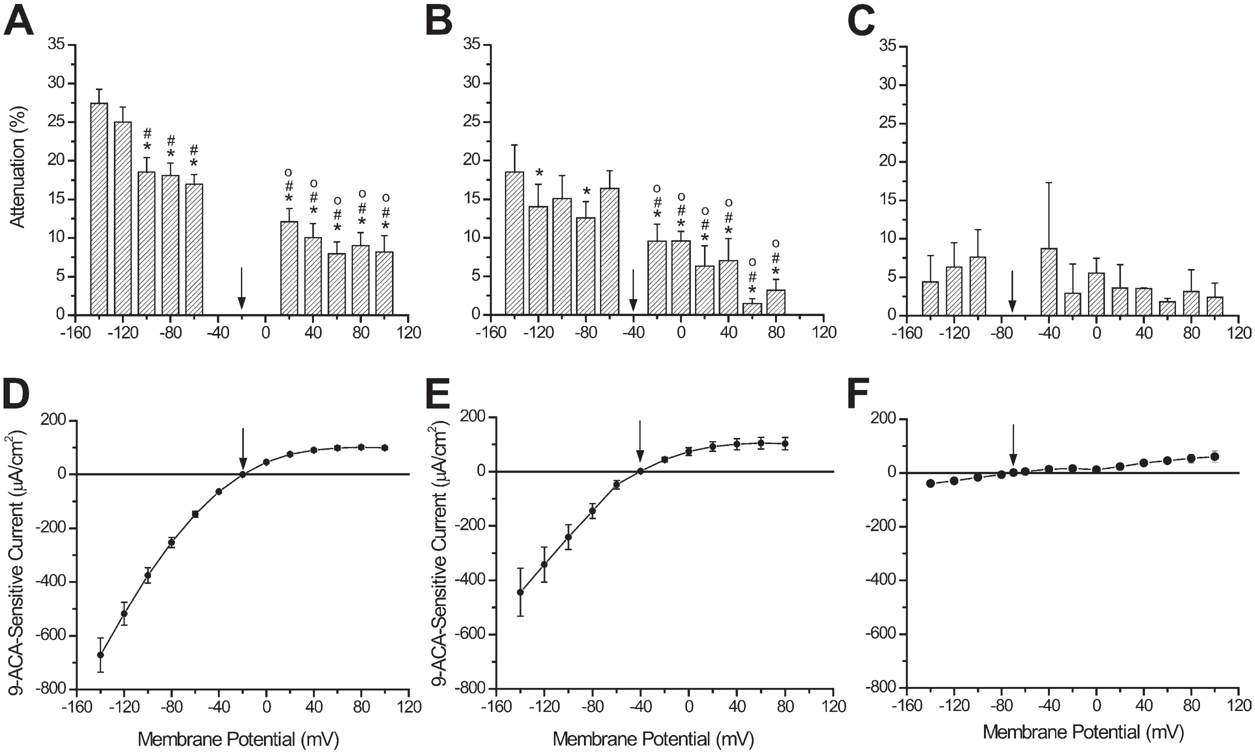

Figure 7. Voltage-dependence of average attenuation and 9-ACA-sensitive I_Cl's at various $[\mathrm{Cl}]_\mathrm{i}$. (A–C) Graphs show the voltage dependence of the maximal attenuation obtained from fibers equilibrated with 70 mM (V_H = −20 mV, n = 8); 40 mM (V_H = −40 mV, n = 4), and 10 mM (V_H = −70 mV, n = 3) $[\mathrm{Cl}]_\mathrm{i}$, respectively. The maximal peak attenuation (at −140 mV) was 27.4 ± 1.8% and 18.5 ± 3.5% for 70 and 40 mM $[\mathrm{Cl}]_\mathrm{I}$, respectively. Statistical significance with respect to peak attenuation values at −140 mV is denoted by *. Statistical significance with respect to values at −120 mV is denoted by #. The symbol o indicates significance with respect to all data at negative voltages. D–F are the corresponding plots of the peak 9-ACA–sensitive I_Cl obtained from the same fibers as in A–C, respectively. The error bars represent SEM. V_H values are indicated by the arrows.

the presence of the large tail currents shown in Fig. 8 B. As expected, the optical transients become less affected by smaller outward currents elicited by pulses to less negative potentials (blue and green traces), or even positive potentials (blue and orange traces). An interesting observation (which became possible by using the three-pulse protocol) is that, though P3 is constant, the optical transients immediately following the transition from P2 to P3 are quite variable, and actually depend on the preceding voltage at P2. The most reasonable explanation for this phenomenon is that the optical signals arise from a membrane compartment that is not instantly polarized to a set value (P3), but to a value that depends on the magnitude and direction of the tail currents occurring at the transition between P2 and P3. Since chloride channels rapidly deactivate for large hyperpolarizations, it is conceivable then that the black trace in Fig. 8 A is the least affected in the transition between P2 and P3. In contrast, the orange trace at the same point is the most distorted because it is associated with the largest tail current at the P2–P3 transition (Fig. 8 B) coming from a positive P2 (no deactivation). The above arguments are confirmed by observing that blocking I_{Cl} with 9-ACA (Fig. 8, C and D) results in more rectangular di-8-ANEPPS transients (Fig. 8 C). In other words, with the application of 9-ACA, all the current-dependent effects on the optical traces have subsided, including the aforementioned variability in the portion of the signals associated with the fixed pulse P3.

Another interesting feature of the optical records shown in Fig. 8 (A and C) is that they illustrate the great stability of the muscle fiber preparation. Notably, when most of the current was blocked by 9-ACA, the di-8-ANEPPS transients observed during the prepulse to +80 mV (six of them are shown superimposed in Fig. 8 C) did not change significantly with respect to those in control conditions (six of them superimposed in Fig. 8 A). This proves that there was very little rundown during the experiment.

Fig. 8 (E and F) shows model predictions of the average TTS voltages and currents, respectively, in response to the same three-pulse stimulation used in the experiment while assuming (as done previously in Fig. 4) that there is an equal distribution of P_{Cl} (in this case 2.7 × 10^{-5} cm/s) in the sarcolemma and TTS membranes. It can be observed, as previously shown for single-pulse

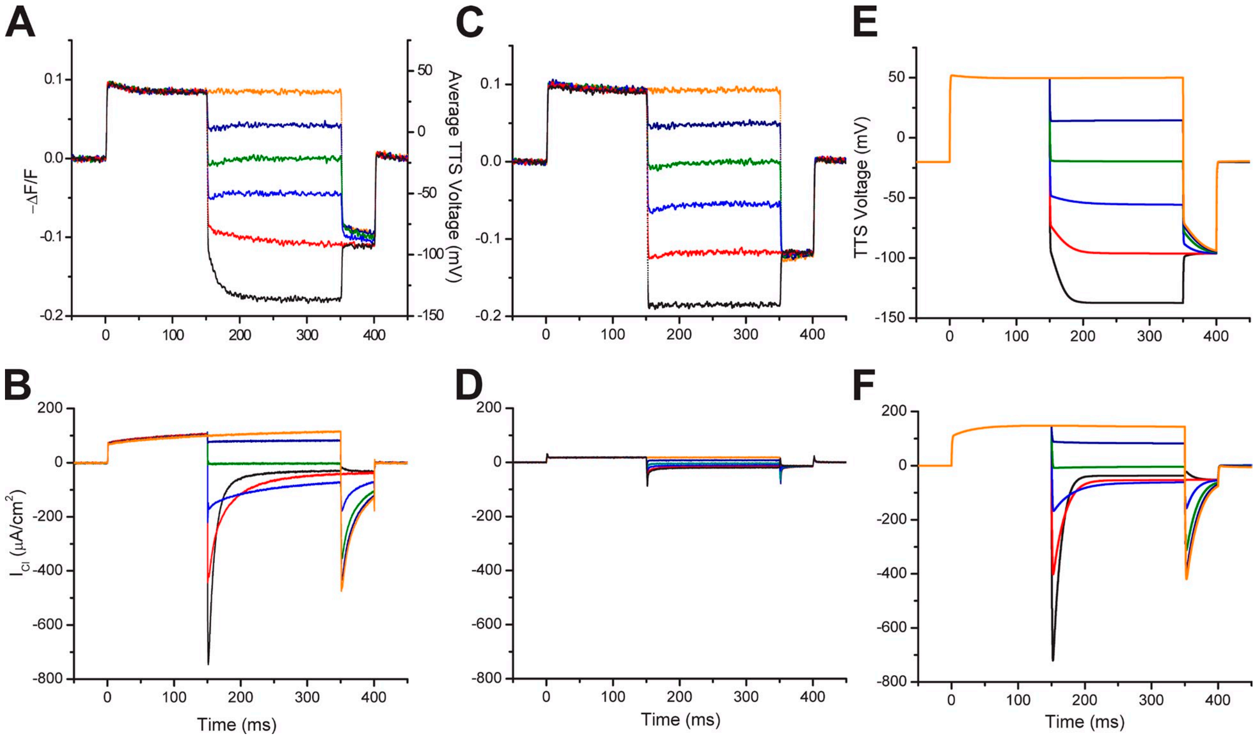

Figure 8. Currents and di-8-ANEPPS transients elicited in response to a three-pulse stimulation protocol (data and model simulations). (A) Di-8-ANEPPS transients recorded under control conditions in response to three-pulse stimulation (see Materials and methods). The test pulses were −120, −80, −40, 0, 40, and 80-mV pulses from V_H = −20 mV (black, red, blue, green, dark blue, and orange traces, respectively). The deconvolution of ΔF/F (left vertical axis) into membrane potential (right vertical axis) was done according to the regression formula $V_m = (\Delta F/F - 0.035)/1.6 \times 10^{-3}$ (in mV). (B) Current traces recorded using the same pulses as in A. (C) Di-8-ANEPPS transients recorded in the presence of 9-ACA in response to the same protocol as in A. (D) Current records (residual current) using the same pulses as in A in the presence of 9-ACA. (E) Model predictions of the TTS membrane potential assuming equal chloride permeability density in the TTS and surface membranes and the geometrical parameters of the fiber (see below). (F) Ionic currents associated with the simulated traces in E. Fiber parameters: radius = 31 μm; length = 372 μm; capacitance: 5.7 μF/cm².

stimuli, that the model reproduces very accurately the main features of the experimental data; namely the voltage transitions during the test pulses (P2) display the characteristic attenuation at the onset of large hyperpolarizations and more rectangular time courses for less negative or positive P2. At the same time, the main features (kinetics, magnitude, and voltage dependence) of I_{Cl} records are well predicted by the model. Perhaps the most interesting aspect of the model simulations for three-pulse stimuli is the great similarity with the data at the transition between P2 and P3. As noted in Fig. 8 E, the predicted time course of the average TTS voltage also departs from the rectangular transition for the simulations of the voltage-clamp transition from +60 to −100 mV (magenta trace), whereas it is almost undistorted for the −140 to +100 mV transition (black trace).

Currents and relative open probability of ClC-1 investigated with three-pulse protocols in multiple fibers: effects on optical transients

Fig. 9 A is an I-V plot of the average 9-ACA–sensitive peak I_{Cl} recorded from fibers internally equilibrated with 70 mM $[Cl]_i$. It displays the characteristic inward rectification of ClC-1 channels with a value of 710 ± 127 $\mu A/cm^2$ ($n = 5$) for the most negative P2 tested (to −140 mV) and an asymptotic value of 107 ± 15 $\mu A/cm^2$ for the most positive P2 tested (to +60 mV). An important benefit of the three-pulse protocol used in these experiments is that it provides an easy method to evaluate the voltage dependence of the steady-state activation of ClC-1 by determining its relative P_O (Pusch et al., 1995, 2000). Fig. 9 B shows this voltage dependence as calculated from the same experiments as above. The data were fitted with a Boltzmann curve,

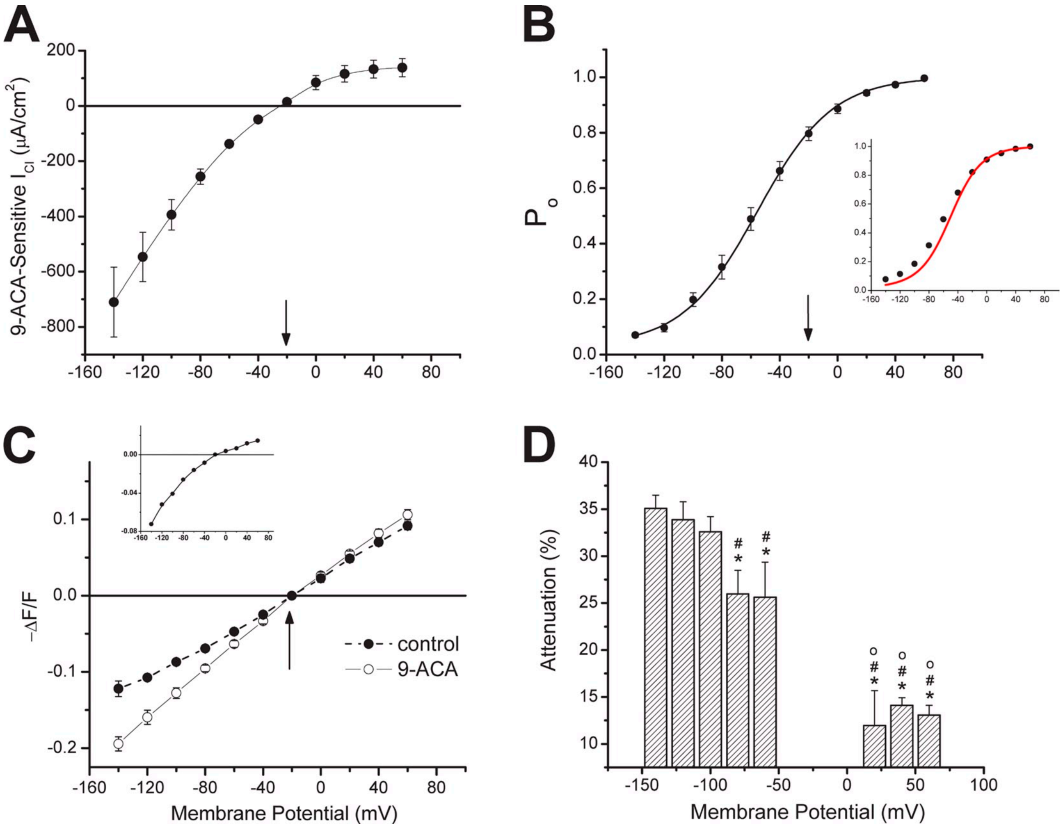

Figure 9. Voltage dependence of average I_{Cl}, P_O, fluorescence changes, and attenuation obtained from fibers stimulated with the three-pulse protocol. (A) Plot of the average peak 9-ACA–dependent I_{Cl} as a function of V_m at P2. (B) Relative P_O was obtained from current tails at the onset of P3 and is plotted versus V_m at P2. The solid line corresponds to the Boltzmann fit to the data. The red trace in the inset is the $h_\infty(V)$ function in the TTS model calculated with the parameters listed in the Table A2 of the Appendix, except that $\bar{\alpha} = 0.04$ ms^{-1}, $k_\alpha = 47$ mV, and $V_\beta = -100$ mV. The black symbols in the inset are P_O values calculated from model simulations of I_{Cl} using an identical open channel chloride permeability ($P_{Cl} = 2.7 \times 10^{-5}$ cm/s) at the surface and TTS membrane compartments (the fiber radius was assumed to be 26 µm). (C) The solid and open circles are the ΔF/F changes in di-8-ANEPPS fluorescence recorded early during P2 in the absence and presence of 9-ACA, respectively, are plotted versus V_m at P2. The ΔF/F difference between average data points (9-ACA minus control) are plotted in the inset. (D) Average peak attenuations (%) at various P2 are plotted versus V_m at P2. The data in this figure were obtained from five fibers voltage clamped at $V_H = -20$ mV. The arrows in each graph indicate V_H. Statistical significance with respect to peak attenuation values at −140 mV is denoted by *. Statistical significance with respect to values at −120 mV is denoted by #. The symbol o indicates significance with respect to all data at negative voltages.

$$P_O = \frac{1}{\left(1 + e^{-\left(\frac{V_m - V_{1/2}}{k}\right)}\right)},$$

in which $V_{1/2}$ was -58 ± 11 mV and k was 27 ± 3 mV ($n = 5$). It should be noted that V_m in this expression is the membrane potential of the surface membrane (as recorded by the voltage electrode) during the test pulse (P2). But, as discussed previously, the surface membrane potential differs from that of the TTS membrane. Thus, it is pertinent to ask what the actual voltage dependence of P_O is for channels located in the TTS. To address this question, we calculated from model simulations what $h_\infty(V)$ function in the TTS (see Appendix) reasonably predicts the voltage dependence recorded experimentally as shown in Fig. 1 C. The results of these simulations (Fig. 1 C, inset) suggest that due to the attenuation in TTS voltages, the steady-state voltage dependence of P_O measured in muscle fibers (closed symbols in inset) is less steep (particularly at more negative potentials) than the intrinsic steady-state voltage dependence of the ClC-1 channels in the TTS (continuous red line in inset). A corollary of these observations is that to accurately assess the actual steady-state voltage dependence of activation of ClC-1 channels in muscle fibers, P_O should be calculated from data obtained in conditions in which I_{Cl} is as small as possible.

Fig. 9 C is a plot of the average ΔF/F change, measured early after the P1 to P2 transition when using the three-pulse protocol, as a function of the membrane potential in P2. The open symbols and the linear regression line through the data points illustrate the linearity of the transients after blocking I_{Cl} with 9-ACA. In contrast, the solid symbols show a nonlinear voltage dependence of the ΔF/F changes measured under control conditions. In addition, due to the presence of I_{Cl}, the control data points are smaller than the 9-ACA points at every membrane potential, and the differences between them are larger in the hyperpolarizing direction than for positive voltages. The inset in Fig. 9 C shows the voltage dependence of the differences between both datasets. The similarity with the current plot in Fig. 9 A features is remarkable, again illustrating that the TTS voltage changes are attenuated due to the presence of I_{Cl}. This is further reinforced by the actual measurements of the peak attenuation, plotted as a function of the membrane potential in Fig. 9 D. These results are similar to those obtained at the same $[Cl]_i$ but using a single-pulse protocol, as shown in Fig. 7 A. However, the three-pulse protocol provides evidence of robust attenuations, reaching a value of $35.1 \pm 1.4\%$ at $V_m = -140$ mV, which most likely results from the large peak currents observed at the onset of P2.

DISCUSSION

There is a consensus in the literature that ∼70–80% of the resting conductance in mammalian skeletal muscle fibers is contributed by the chloride conductance (Bretag, 1987). Nonetheless, to understand the detailed role of this conductance in normal and diseased animals, the quantitative distribution of chloride channels between the surface and TTS membranes must be known. Although electrophysiological experiments have led to the suggestion that a large fraction of the chloride conductance may be located in the TTS membranes (Palade and Barchi, 1977; Dulhunty, 1979; Coonan and Lamb, 1998; Dutka et al., 2008), there is contradicting immunohystochemical evidence questioning the idea that ClC-1 might be expressed in the membranes of TTS (Gurnett et al., 1995; Papponen et al., 2005). Altogether, the voltage dependence and kinetics of 9-ACA–sensitive currents, and the attenuation effects that these currents have on di-8-ANEPPS potentiometric signals, provide strong confirmatory evidence that a large fraction of functional ClC-1 channels are present in the TTS. Although we cannot offer a firm explanation for the discrepancy between our functional data and immunohystochemical data, we believe that the latter are not conclusive. The use of cross sections of whole muscles (Gurnett et al., 1995; Papponen et al., 2005) does not seem to be the best approach to assess for the presence of ClC-1 in the TTS. Immunohystochemical evaluation of longitudinal sections would be more desirable. In addition, the biochemical and immunohystochemical studies used antibodies raised only against one epitope in the C terminus of ClC-1 (Gurnett et al., 1995; Papponen et al., 2005). As suggested by Aromataris and Rychkov (2006), it is possible that ClC-1 channels expressed in the TTS may hide this epitope (through interactions with native TTS proteins) from the accessibility to antibodies. Alternatively, posttranslational processing of the C terminus of ClC-1 could occur in the TTS, as already demonstrated for the dihydropyridine receptor channel (De Jongh et al., 1991). Obviously, the use of antibodies targeted to other epitopes of ClC-1 would resolve these latter issues.

The present paper aims to respond quantitatively the following question: what is the specific distribution of ClC-1 between the surface and TTS membrane in mammalian skeletal muscle fibers? We used enzymatically dissociated fibers in which both membrane systems are preserved intact as indicated by their very small unspecific leak currents ($<12\ \mu A/cm^2$) and large membrane capacitance ($>5\ \mu F/cm^2$). This is in contrast with other approaches used to investigate this issue in which the integrity of the fibers was compromised by eliminating either the TTS or the surface membrane (Palade and Barchi, 1977; Coonan and Lamb, 1998). Although the so-called detubulation procedures have been used in the past to evaluate the distribution of conductances between surface and TTS membranes (Eisenberg and Gage, 1967, 1969; Heiny and Vergara, 1982), their deleterious side effects on mammalian fibers' properties put in jeopardy the conclusions reached (Dulhunty, 1982). Alternatively, estimations of the electrical properties of the TTS in skinned fibers (removing the sarcolemma) are indirectly based on measurements of tension development at various ionic conditions (Coonan and Lamb, 1998); in our opinion, this approach unduly relies on the preservation of a series of steps in the excitation–contraction coupling process.

Since the TTS is not accessible to direct electrical measurements, we used the fluorescent potentiometric indicator di-8-ANEPPS, which is a nonpenetrating probe, undergoing very rapid changes in electrochromicity in response to transmembrane voltage changes (Loew, 1993). It has been previously demonstrated that this dye has low toxicity (Kim and Vergara, 1998b), and it noninvasively provides information about average voltage changes in the TTS of skeletal (Kim and Vergara, 1998a, b; DiFranco et al., 2005) and cardiac muscle fibers (Huser et al., 1996). We also demonstrate here that, as shown in Fig. 8, almost no rundown was detected in fibers studied for 40–60 min, when exposed to repeated illumination for periods of up to one second. This observation assured us that changes seen before and during 9-ACA application were due to I_{Cl} blockage and not to uncontrolled side effects.

The use of a two-microelectrode voltage clamp, rather than a patch-clamp system, was technically important to avoid the problem of artifactual current-dependent attenuations in the assessment of the membrane voltage by the patch pipette. As expected, the kinetics and magnitude of voltage records, measured in our case by an independent micropipette, were not affected by the presence or absence of chloride currents (Figs. 2, A and B, insets, respectively). An additional potential source of error is the voltage attenuation along the longitudinal axis of the fiber due to its cable properties. For a typical fiber with radius and length of 25 and 400 µm, respectively, and an internal resistivity (R_i) of 150 Ωcm, the short cable model of a muscle fiber (Bezanilla et al., 1982) predicts that peak currents of ~800 µA/cm^2 (within the range of those recorded at −140 mV) would result in voltage deviations at the fiber's ends (with respect to that of the voltage pipette) of ~12%. Under these conditions, only a fraction of these deviations (<4%) is predicted for longitudinal distances of <25 µm from the voltage recording micropipette. We have previously verified that short cable model predictions (Bezanilla et al., 1982) are approximately confirmed using exploratory micropipettes in voltage-clamped fibers (Woods et al., 2005). To minimize the impact of voltage attenuation errors in our optical records, we took the precaution that the di-8-ANEPPS measurements were made within a radius of ~20 µm of the voltage micropipette. Nevertheless, errors introduced by the cable properties of the muscle fibers affect the accuracy of I_{Cl} measurements as well. In fact, these errors are likely to be important contributors to the progressive increase in size of the error bars (SEM) at large hyperpolarizations, as shown in I-V curves (Figs. 7 and 9). From the short cable model equations, we estimate that, due to voltage dropouts along the cable, the largest currents reported in this paper (800–900 µA/cm^2) are subject to ~10% uncertainty (Bezanilla et al., 1982).

As shown previously, a critical requirement to quantitatively calculate the changes in TTS membrane potential underlying the optical signals is that reliable regression lines (e.g., Fig. 1) can be obtained for every experiment (DiFranco et al., 2005). We must also establish the equivalence between optical data and model predictions of the TTS membrane potential changes. To this end, we have adopted the well-documented assumption that optical signals represent a weighted average of the TTS membrane voltage changes (Heiny and Vergara, 1982, 1984; Heiny et al., 1983; Kim and Vergara, 1998b; DiFranco et al., 2005). In support of this assumption, we verified that model predictions of the weighted average TTS membrane potential coincide with those calculated from di-8-ANEPPS signals in passive fibers (unpublished data). We further confirmed that the kinetic properties of the optical transients at the onset and end of step voltage-clamp pulses are well predicted by model simulations of the TTS under passive conditions (unpublished data).

We demonstrated that robust I_{Cl} could be detected in fibers with 40 and 70 mM [Cl]$_i$. The similarity between our I_{Cl} records, in terms of 9-ACA sensitivity, kinetic properties, and voltage dependence, and those published by other laboratories (Fahlke and Rudel, 1995; Fahlke et al., 1996; Rychkov et al., 1996; Lueck et al., 2007) provides an undeniable validation that we are reporting on fluxes through ClC-1 channels. We first used single-pulse stimulation because it allowed us to analyze in simpler terms the effects of this current on the TTS membrane potential. As illustrated in Figs. 2 and 3, ionic currents recorded with this pulse protocol from fibers clamped at V_{Cl} with 40 and 70 mM [Cl]$_i$ display the main features of I_{Cl} currents. At the same time, TTS optical signals clearly demonstrate time-dependent attenuations (Fig. 3 A and Fig. 4 A) that are associated with the presence of I_{Cl} (Fig. 3 C and Fig. 4 D), particularly in response to large hyperpolarizations, which disappear after I_{Cl} blockage (Fig. 3 B). Furthermore, the data in Fig. 7 demonstrate that both I_{Cl} and the peak attenuation of optical records are significantly larger in fibers equilibrated in 40 and 70 nM [Cl]$_i$ than those recorded in the presence of 10 mM Cl$_i$. This fact provides the ultimate support to the concept that the peak attenuation observed in di-8-ANEPPS transients depends on the magnitude of I_{Cl}. Our I_{Cl}s, measured using the three-pulse protocol in fibers equilibrated in 70 mM $[Cl]_i$ (Fig. 8), have similar appearance and voltage dependence as those previously described by other authors (Fahlke and Rudel, 1995; Rychkov et al., 1996; Lueck et al., 2007). Nonetheless, the largest 9-ACA–sensitive I_{Cl} reported here in response to −120-mV pulses (722 ± 163 µA/cm^2), when converted into equivalent units (139 ± 31 pA/pF), are approximately threefold the 49 ± 4 pA/pF reported by another laboratory, also for flexor digitorum brevis fibers (Lueck et al., 2007). This disagreement may be explained by differences in the age of the mice used (18–20 d in their case vs. 14–15 wk in ours) and/or the voltage-clamp technique used (whole-cell patch clamp vs. two microelectrodes).

We operationally characterized a time-dependent attenuation variable to evaluate the fractional difference between optical records obtained (at every potential) before and after the application of 9-ACA (Fig. 5). Since this variable is normalized with respect to signals obtained under passive conditions, it allows us to compare data obtained from different experiments, as illustrated in Figs. 7 and 9. An important comparative outcome from the data shown in these figures is that signals recorded with the three-pulse stimulation protocol yielded significantly larger ($P < 0.05$) peak attenuations at −140 mV (35.1 ± 1.4%) than those observed at the same ionic conditions from the single-pulse protocol (e.g., 27.4 ± 1.8% at −140 mV).

A central feature in this paper is our ability to predict the actual properties of di-8-ANEPPS transients, representative of a weighted average of the TTS membrane potential changes, with realistic computer simulations. As shown in the Appendix, the radial cable model equations, stipulating the existence of an access resistance (R_s) in series with the TTS, were modified from the original equations of Adrian and collaborators (Adrian et al., 1969; Adrian and Peachey, 1973), but modified to include time- and voltage-dependent conductances (Heiny et al., 1983; Ashcroft et al., 1985). In the current paper, as explained in the Appendix, the radial cable elements include a descriptive model of the chloride channel ClC-1. In addition, the model contemplates a diffusion equation, modified from Barry and Adrian (1973; Friedrich et al., 2001), to predict chloride concentration changes in the lumen of the T-tubules resulting from chloride fluxes at each radial segment of the TTS. Both the radial cable model and diffusion equations were integrated simultaneously using conventional numerical methods (see Appendix). It is important to note, however, that the hypothetical two-state model for generating chloride currents at each segment of the radial cable, and at the sarcolemma, was only intended to provide an approximate behavior of the actual properties of the currents through ClC-1 channels. As shown in Fig. A1 in the Appendix, for each membrane element of the TTS, this model of the ClC-1 channel is capable of generating inwardly rectifying currents that rapidly deactivate in response to large hyperpolarizations (from V_H), and smaller and slower currents for smaller hyperpolarizing pulses and for depolarizing pulses. Interestingly, the features of the overall chloride currents generated by integration of model equations are very similar to those reported by other authors (Fahlke et al., 1996; Lueck et al., 2007) and predict quite well our own electrophysiological data. However, this finding may be fortuitous since an important caveat of the two-state model is that it implies a predetermined influence of the luminal [Cl] on the properties of the currents. As explained in the Appendix, the model assumes that open channels intrinsically rectify due to the presence of a chloride binding site at the external mouth of the channel and that the actual state of the ClC-1 channel is controlled by a simple voltage-dependent gate (h). Unfortunately, there is not experimental information so far supporting this hypothetical assumption. It will be interesting in the future to investigate how well the model calculations predict the overall features of I_{Cl}, including its dependence on the external [Cl].

There are two (related) questions that remain to be answered regarding the distribution of P_{Cl} between the sarcolemma and TTS membranes: (1) what is the actual range of P_{Cl} densities that account for our data; and, (2) what are the respective contributions of the sarcolemma and the TTS membrane I_{Cl} currents to the total I_{Cl} record. Although the answer to these questions seems to be already provided in the paper, given the excellent predictions of the experimental data by model simulations while presuming an equal P_{Cl} density distribution, we should explore other options that might be compatible with the fiber-to-fiber variability in the data. Fortunately, our measurements of peak attenuation (i.e., the maximal reduction in amplitude of optical records at the peak of the inward currents) allow us to contrast the dispersion of data from multiple fibers (as shown in Figs. 7 and 9) with model simulations for a range of channel distributions. Since the attenuation is nonlinearly dependent on the magnitude of P_{Cl}, and other fiber parameters, we focused on predicting the effects of varying the density of P_{Cl} in the TTS (between 0 and 100%) on the peak attenuation and 9-ACA–sensitive I_{Cl} as they would be observed at the onset of P2 = −120 mV in an average fiber (51 µm in diameter). Since the idea is to compare model predictions with the results shown in Fig. 9 (A and D), it was necessary that 9-ACA–sensitive I_{Cl} remains constant at ~710 µA/cm^2. The attenuation predicted by the model (Fig. 10 A, open symbols) is plotted versus the percentage proportion of P_{Cl} in the TTS. For comparison, the experimental attenuation (Fig. 9 D) observed at −140 mV (35%, solid black symbol) and its corresponding error bar (±1.4%) are shown superimposed with the model predictions. It can be

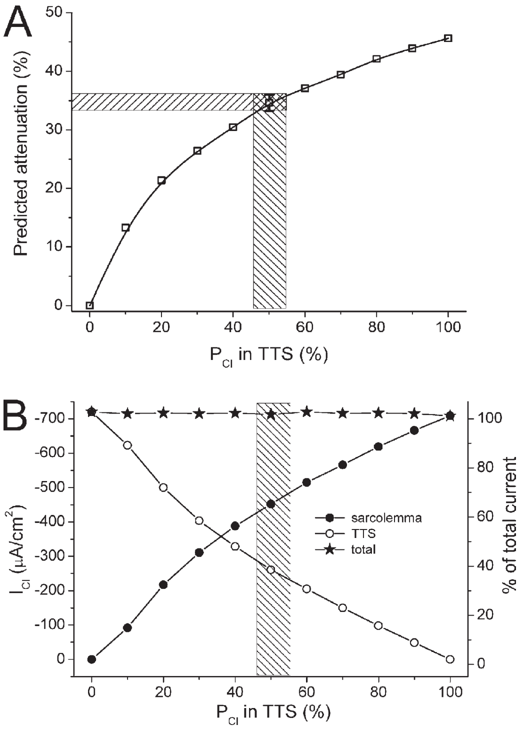

Figure 10. Model calculations of the attenuation and surface and TTS components of I_{Cl} for various distributions of P_{Cl}. (A) Predicted percentage attenuation (open squares) plotted as a function of the percentage P_{Cl} in the TTS. (B) Total (solid stars), sarcolemma (solid circles, shown as % of total), and TTS (open circles, shown as % of total) chloride currents calculated for various percentages of P_{Cl} in the TTS. Note that the left ordinate axis is inverted (negative currents are drawn upward). The fiber radius was 25.5 μm; model parameters (other than P_{Cl}) were those in Tables 1 and 2 of the Appendix. Specific values of P_{Cl} (in cm/s) for the surface and TTS membranes, respectively, for every percentage distribution in the TTS (in parenthesis) were: 0 and 4.96×10^{-5} (100%); 5.05×10^{-6} and 4.55×10^{-5} (90%); 1.02×10^{-5} and 4.1×10^{-5} (80%); 1.56×10^{-5} and 3.64×10^{-5} (70%); 2.16×10^{-5} and 3.25×10^{-5} (60%); 2.78×10^{-5} and 2.78×10^{-5} (50%); 3.45×10^{-5} and 2.3×10^{-5} (40%); 4.2×10^{-5} and 1.38×10^{-5} (30%); 5.2×10^{-5} and 1.3×10^{-5} (20%); 6.66×10^{-5} and 7.4×10^{-6} (10%); 7.5×10^{-5} and 0 (0%).

observed that the average experimental attenuation is predicted if an equal distribution of P_{Cl} (50%) in the surface and TTS membranes is assumed. If the uncertainty introduced by the SEM of the data are taken into account, an attenuation range from 33.7 to 36.5% can be predicted (hatched horizontal area Fig. 10 A). In turn, the interpolation of these limits in the plotted data and further extrapolation on the abscissa, suggests a range from 46 to 65% of the total P_{Cl} permeability must be in TTS to explain the experimentally observed attenuations. For the same simulation, Fig. 10 B shows the surface (solid circles) and T-tubular (open circles) components of the total peak I_{Cl} (solid stars) predicted for a different percentage proportion of P_{Cl} in the TTS. It can be observed that for the 50% permeability distribution, which approximately explains the 35% average attenuation in the optical data, the surface membrane and TTS current contributions to the total I_{Cl} were 258 μA/cm^2 (36%) and 452 μA/cm^2 (64%), respectively. Moreover, within the 46–65% range of P_{Cl} distributions (hatched vertical box), the TTS membranes contribute between 60 and 68% of the total chloride current. When the same analysis is performed for the data in Fig. 7 A, from the range of P_{Cl} distributions we calculate that TTS membranes contribute between 40 and 53% of the total I_{Cl}. Overall, the optical data would be consistent with a relatively broad range of current contributions from the TTS. Ultimately, more experiments will be necessary in the future to refine the actual numbers, but we must note that, given the intrinsic noise in the di-8-ANEPPS optical records, the measurements of peak attenuation are likely to be more accurate under conditions in which larger currents are attained (e.g., three-pulse experiments, 70 mM $[Cl]_i$). However, it is also possible that fiber-to-fiber differences in the actual density of ClC-1 channels in each membrane compartment (sarcolemma and TTS) may contribute to the observed variability in peak attenuation for comparable values of total I_{Cl}. The methodology used in this paper could help to decide if this is the case. Regardless of the outcome, it is safe to state at this point that a significant portion (∼50%) of the ClC-1 currents arise from the TTS membranes.

APPENDIX

Radial cable model equations for the TTS of mammalian skeletal muscle fibers including a chloride conductance and ion diffusion

We followed the nomenclature reported previously (Ashcroft et al., 1985; Kim and Vergara, 1998b; DiFranco et al., 2008) and the assumption (Adrian and Peachey, 1973) that the lumen of the TTS is separated from the extracellular fluid by an access resistance (R_s, in Ωcm^2). The partial differential equation that governs the radial (r) and time (t) dependent changes in T-tubule membrane potential ($u(r,t)$) in response to voltage changes at the external boundary is (Adrian et al., 1969)

$$\frac{\partial^2 u}{\partial R^2} + \frac{1}{R}\frac{\partial u}{\partial R} = \nu^2 u + \frac{\partial u}{\partial t}, \tag{A1}$$

where a is the radius of the muscle fiber, $R = r/a$, $T = \bar{G}_L t / (\bar{C}_w a^2)$ and $\nu = a\sqrt{\bar{G}_w / \bar{G}_L}$. In these equations, the parameters $\bar{C}_w$ and $\bar{G}_w$ are the capacitance (in μF/cm^3) and conductance (in S/cm^3) of the tubular membrane per unit volume of muscle fiber, respectively, and $\bar{G}_L$ is the effective radial conductivity (in S/cm). If ρ is the fraction of the total muscle volume occupied by T-tubules, σ is a TTS tortuosity factor, and ξ is the volume-to-surface ratio of T-tubules, then (Adrian et al., 1969)

$\overline{C}_w = C_W\,\rho/\xi$; $\overline{G}_w = G_W\rho/\xi$; and $\overline{G}_L = G_L\rho\sigma$, where C_w and G_w are the TTS membrane capacitance (in µF/cm^2) and conductance (in S/cm^2) per unit TTS membrane area, and G_L is the specific T-tubule lumen conductivity (in S/cm). Numerical integration methods are necessary to solve Eq. A1, and to predict the voltage of TTS cable elements, when nonlinear conductances are assumed to be in parallel with capacitive elements (Adrian and Peachey, 1973; Heiny et al., 1983; Ashcroft et al., 1985). In this case, we replace the term v^2u in Eq. A1 with the more general term

$$a^2\,\frac{\overline{I_W}(u,r,t)}{\overline{G_L}}$$

where $\overline{I_W}(u,r,t)$ is a generalized current normalized per volume of fiber. Keeping the same definitions for R and T, Eq. A1 is transformed into

$$\frac{\partial^2 u}{\partial R^2} + \frac{1}{R}\frac{\partial u}{\partial R} = a^2\,\frac{\overline{I_W}}{\overline{G_L}} + \frac{\partial u}{\partial T}. \tag{A2}$$

For the simulations in this paper we assumed that $\overline{I_W}(u,R,T)$ is exclusively contributed by chloride ions flowing across the TTS walls. Thus,

$$\overline{I_W}(u,R,T) = I_{Cl}(u,R,T)\frac{\rho}{\zeta}, \tag{A3}$$

where $I_{Cl}(u,R,T)$ is the chloride current per cm^2 of TTS membrane.

Our approach to simulate the kinetics and voltage dependence of I_{Cl} at each radial cable element was based on the following hypothetical model (Klein, 1985). (a) The chloride channel has two states, open and blocked (or deactivated). (b) The permeability (P_{Cl}) of the open chloride channel is constant (in cm/s), and the current through it is described by constant-field theory (Goldman, 1943) with the inclusion of a term that implies a reduced chloride concentration ($[\mathrm{Cl}]_m$) instead of the bulk value $[\mathrm{Cl}]_o$; this has been hypothesized as a screening effect due to surface membrane charges (Klein, 1985), but it may represent the restrictive effect of an external binging site of the channel. Under these conditions,

$$I_{Cl-open}(V) = \tag{A4}$$

$$P_{\mathrm{Cl}}\cdot\frac{(V-V')\cdot F^2}{RT}\cdot \frac{\left\{[Cl]_o\cdot\exp\left(\left.(V-V')\cdot F\middle/RT\right.\right)-[Cl]_i\cdot\exp\left(-\left.(V-V')\cdot F\middle/RT\right.\right)\right\}}{\left\{1-\exp\left(-\left.(V-V')\cdot F\middle/RT\right.\right)\right\}},$$

where

$$V' = \frac{RT}{F}\cdot\ln\left(\frac{[\mathrm{Cl}]_m}{[\mathrm{Cl}]_o}\right).$$

R, T, and F are the usual thermodynamic constants (note that R and T here are not the normalized radial and time variables used above). (c) The time and voltage dependence of I_{Cl} at each radial cable element is accounted for by the equation

$$I_{Cl}(V,t) = I_{Cl-open}(V)\cdot h(V,t), \tag{A5}$$

in which h represents the probability of the channel being open, and the transition from open to blocked state is calculated from the differential equation:

$$\frac{dh(V,t)}{dt} = \alpha(V)\cdot(1-h) - \beta(V)\cdot h. \tag{A6}$$

The variables α and β are voltage-dependent kinetic rate constants for the state variable h. The equations for α and β are

$$\alpha(V) = \frac{\bar{\alpha}}{1+\exp\left(-\dfrac{V-V_\alpha}{k_\alpha}\right)}\ ;\ \beta(V) = \frac{\bar{\beta}}{1+\exp\left(\dfrac{V-V_\beta}{k_\beta}\right)} \tag{A7}$$

(d) As usual, from Eq. A6,

$$\tau(V) = \frac{1}{\alpha(V)+\beta(V)}\ \text{and}\ h_\infty(V) = \frac{\alpha(V)}{\alpha(V)+\beta(V)}.$$

(e) It follows from above that the steady-state I_{Cl} in each cable element of a fiber voltage clamped at a holding potential V_H can be calculated as

$$I_{Cl-rest}(V_H) = I_{Cl-open}(V_H)\cdot h_\infty(V_H). \tag{A8}$$

(f) Typical values of the parameters used to calculate I_{Cl} as a function of voltage and time are included in Table A2. Fig. A1 shows the main features of the peak and steady-state open channel currents (Fig. A1 A, solid and dashed traces, respectively) as they are calculated at

TABLE A1

Specific parameter values for passive radial cable

Parameter	Value	Dimension
a	20–30	µm
C_W	1.0	µF/cm^2
G_L	11.3	mS/cm
R_s	40	Ωcm^2
ρ	0.004	
ξ	1.1×10^{-6}	cm
σ	0.32	
D_{Cl}	1×10^{-5}	cm^2/s

every element of the radial cable model. Fig. A1 B shows the voltage dependence of the characteristic parameters $h_\infty(V)$ and $\tau(V)$ (solid and dashed traces, respectively) for the I_{Cl} model using the values included in Table A2.

Chloride diffusion in the TTS lumen

Changes in luminal chloride concentration in the TTS ($[Cl]_o$) occurring in response to the current flow across the T-tubule walls were calculated from simultaneous integration of the diffusion equation (Barry and Adrian, 1973; Friedrich et al., 2001):

$$\frac{\partial[Cl]_o(r,t)}{\partial t}=\frac{\sigma D_{Cl}}{r}\frac{\partial}{\partial r}\left[\frac{r\partial[Cl]_o(r,t)}{\partial r}\right]-\frac{I_{Cl}(r,t)}{\rho \mathrm{F}}, \tag{A9}$$

where D_{Cl} is the diffusion coefficient of chloride ions in the lumen of the TTS (in cm^2/s), F is the Faraday constant, and I_{Cl} is the chloride current per cm^2 of TTS membranes. Using the dimensionless variables $R = r/a$ and $\tau = \sigma D_{Cl}\, t/a^2$, this equation becomes

$$\frac{\partial^2[Cl]_o}{\partial R^2}+\frac{1}{R}\frac{\partial[Cl]_o}{\partial R}=\frac{\partial[Cl]_o}{\partial \tau}+\frac{I_{Cl}}{a^2\sigma D_{Cl}\rho \mathrm{F}}. \tag{A10}$$

Numerical integration of model equations

TTS voltage. At a given time j, the finite differences approximation of the partial differential equation of the T-tubular voltage (Eq. A2) is (Crank, 1975)

$$\frac{\partial^2 u}{\partial R^2}+\frac{1}{R}\frac{\partial u}{\partial R}\rightarrow\frac{1}{2i\,\delta R^2}\left\{(2i+1)\,u_{i+1}^j-4iu_i^j+(2i-1)u_{i-1}^j\right\}, \tag{A11}$$

where u_i^j is the finite difference representation of the voltage at radial position i at time j, and δR is the normalized distance between shells. The TTS cable is assumed to be made of $n = 60$ radial shells, sealed at the center of the muscle fiber. The finite differences approximation for the time dependence partial differential operator for an arbitrary cable element u_i^j is

$$\frac{\partial u}{\partial T}\rightarrow\frac{u_i^{j+1}-u_i^j}{\delta T},$$

where δR is the dimensionless time interval (Crank, 1975; DiFranco et al., 2007). The external boundary condition ($R = 1$; $i = n$) is (Adrian and Peachey, 1973)

$$\left(\frac{\partial u}{\partial R}\right)_{R=1}=\frac{V_{COM}(t)-u_n^j}{aR_s\bar{G}_L},$$

where $V_{COM}(t)$ is the voltage imposed at the surface membrane of the muscle fiber.

Using an implicit Crank-Nicolson algorithm (Crank, 1975; Gerald, 1978), a finite difference equation for an arbitrary annulus i can be obtained (Kim and Vergara, 1998b; DiFranco et al., 2008):

$$\begin{aligned}&\mathrm{X}\cdot\frac{(2\mathrm{i}+1)}{4\mathrm{i}}\cdot \mathrm{u}_{\mathrm{i}+1}^{\mathrm{j}}-(\mathrm{X}+1)\cdot \mathrm{u}_{\mathrm{i}}^{\mathrm{j}+1}+\mathrm{X}\cdot\frac{(2\mathrm{i}-1)}{4\mathrm{i}}\cdot\\&\mathrm{u}_{\mathrm{i}-1}^{\mathrm{j}+1}=-\mathrm{X}\cdot\frac{(2\mathrm{i}+1)}{4\mathrm{i}}\cdot \mathrm{u}_{\mathrm{i}+1}^{\mathrm{j}}+(\mathrm{X}-1)\cdot\\&\mathrm{u}_i^j-X\cdot\frac{(2\mathrm{i}-1)}{4\mathrm{i}}\cdot \mathrm{u}_{\mathrm{i}-1}^{\mathrm{j}}+a^2\cdot\frac{(\overline{I_{Cl}})_i^j}{\overline{G_L}}\delta T,\end{aligned} \tag{A12}$$

where $(\overline{I_{Cl}})_i^j$ is the current per unit fiber volume (calculated from Eqs. A3 and A5) flowing through the T-tubular element at shell i and at the time interval j during the numerical integration process. Eq. A12 is a recursive formula allowing the calculation of u_i^{j+1} at a time interval δT, while knowing u_i^j. The system of tridiagonal coefficient matrices were solved using a LU decomposition algorithm (Gerald, 1978). The integration of Eq. A6 to update the value of I_{Cl} for every cable element, and for

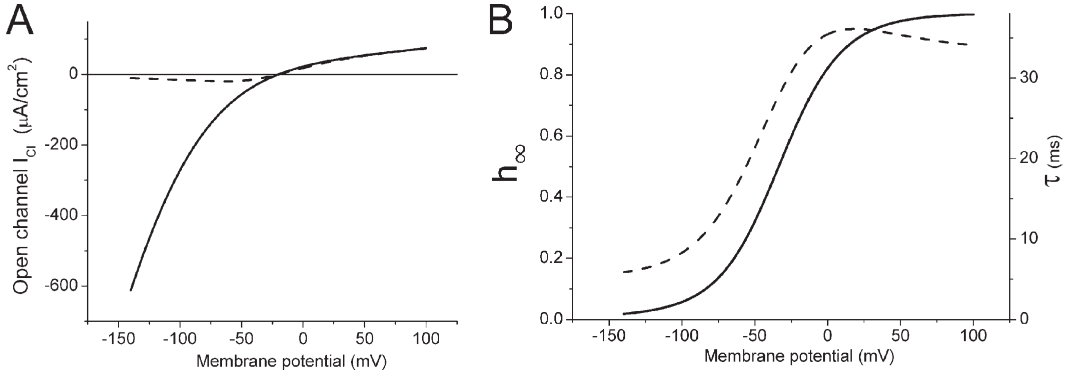

Figure A1. (A) Voltage dependence of peak (solid trace) and steady-state (dashed trace) open channel currents. (B) Voltage dependence of h_∞ (solid trace) and τ (dashed trace).

the surface membrane, was performed with a second order Runge-Kutta algorithm at every time step. The values of the general cable parameters used for the simulations shown in the paper are summarized in Table A1. Specific conductance parameters are given in the figure legends.

Chloride concentration in the lumen of the TTS. The finite difference approximation and Crank-Nicolson algorithm used for the integration of Eq. A10, to calculate the luminal chloride concentration ($[Cl_o]_i^j$) at every shell *i* and at time interval *j*, followed an equivalent rationale to that used for the calculations of u_i^j . Thus, at a given time *j*, the finite differences approximation of the partial differential equation for $[\mathrm{Cl}]_\mathrm{o}$ in the TTS (Eq. A10) is

$$\frac{\partial^2 [Cl]_o}{\partial R^2} + \frac{1}{R}\frac{\partial [Cl]_o}{\partial R} \;\rightarrow\; \frac{1}{2i\delta R^2}\left[(2i+1)c_{i+1}^j - 4ic_i^j + (2i-1)c_{i-1}^j\right],$$

where c_i^j is the finite difference representation of the luminal chloride concentration at radial position *i* at time *j*, and δ*R* is the normalized distance between shells. Also,

$$\left.\frac{\partial c}{\partial \tau}\right|_i^j =: \frac{c_i^{j+1} - c_i^j}{\delta\tau},$$

then,

$$c_i^{j+1} = \qquad \text{(A13)}$$
$$c_i^j + \frac{\delta\tau}{\delta R^2}\left[\frac{c_{i+1}^j(2i+1)}{2i} - 2c_i^j + \frac{(2i-1)c_{i-1}^j}{2i}\right] - \frac{\delta\tau \cdot I_{Cl}}{a^2\sigma D_{Cl}\rho\mathrm{F}}.$$

Eq. A13 allows us to establish recurrence using the Crank-Nicolson algorithm. At the outside boundary ($i = n$), where $[\mathrm{Cl}]_\mathrm{o} = [\mathrm{Cl}]_\text{o-bath}$, we apply Fick's law to the T- tubule's opening:

$$c_n^{j+1} =$$
$$c_n^j + \frac{\delta\tau}{\delta R^2}\left[\frac{(2n+1)\,[Cl]_{o\text{-}bath}}{2n} - 2c_n^j + \frac{(2n-1)c_{n-1}^j}{2n}\right] - \frac{\delta\tau \cdot I_{Cl}}{a^2\sigma D_{Cl}\rho\mathrm{F}}.$$

From (Crank, 1975), we deduce that the boundary condition for the closed end of the TTS network ($i = 0$) is

$$c_0^{j+1} = c_0^j + \frac{4\delta\tau}{\delta R^2}\left[c_1^j - c_0^j\right] + \frac{\delta\tau \cdot I_{Cl}}{a^2\sigma D_{Cl}\rho\mathrm{F}}.$$

Total current and optical signals

The total ionic currents calculated from the integration of the radial cable equations, including the two-state model (I_{Cl}) at each radial cable element of the TTS, was the sum of two contributions: (1) a surface membrane component, calculated from the direct temporal integration of Eq. A5 in response to V_{COM}; and, (2) a TTS component, which encompasses the effective sum of currents originated in this membrane compartment; this was calculated from the application of Kirchhoff laws at the external opening of the TTS (Ashcroft et al., 1985; Kim and Vergara, 1998b), as

$$I_{Cl-TTS} = \frac{V_{COM} - u_n^j}{R_s}, \qquad \text{(A14)}$$

where u_n^j is the voltage across the outermost segment of the TTS at time interval *j*.

Under the assumption that di-8-ANEPPS optical signals occur homogenously at superficial and deep regions of the TTS, and that changes in its optical properties with the transmembrane voltage occur identically at every submicroscopic region of the TTS, then the optical signal obtained within our illumination disk is expected to represent an ensemble average of the voltage contributed by every cable element in the TTS ($\overline{\Delta V_{TTS}}$) weighted by the radius of each annulus (Heiny et al., 1983; Ashcroft et al., 1985; Kim and Vergara, 1998b). This is calculated, for each successive time step, using a numerical trapezoidal integration algorithm based on Simpson's rule (Gerald, 1978) from the formula

$$\overline{\Delta V_{TTS}} = \frac{\int_0^a rV(r)dr}{\int_0^a rdr}.$$

This assumption was used to calculate the predicted optical signals (for comparison with the data) in Figs. 4 and 8 of the paper.

TABLE A2

Typical parameter values for chloride channels

Parameter	Value	Dimension
P_{Cl}	6×10^{-5}	cm/s
$\bar{\alpha}$	0.03	ms^{-1}
V_α	−50	mV
k_α	41	mV
$\bar{\beta}$	0.16	ms^{-1}
V_β	−90	mV
k_β	25	mV
$[\mathrm{Cl}]_\mathrm{m}$	1.5	mM
$[\mathrm{Cl}]_\text{o-bath}$	155	mM
$[\mathrm{Cl}]_\mathrm{i}$	70	mM

See text for specific deviations from these values.

The authors thank Mr. P. Tran for help with the preparation of the manuscript and Mr. R. Serrano for technical support.

This work was supported by National Institutes of Health/National Institute of Arthritis and Musculoskeletal and Skin Diseases grants AR047664 and AR54816.

Edward N. Pugh served as editor.

Submitted: 1 July 2010
Accepted: 29 October 2010

REFERENCES

Adrian, R.H., and S.H. Bryant. 1974. On the repetitive discharge in myotonic muscle fibres. *J. Physiol.* 240:505–515.

Adrian, R.H., and L.D. Peachey. 1973. Reconstruction of the action potential of frog sartorius muscle. *J. Physiol.* 235:103–131.

Adrian, R.H., W.K. Chandler, and A.L. Hodgkin. 1969. The kinetics of mechanical activation in frog muscle. *J. Physiol.* 204:207–230.

Aromataris, E.C., and G.Y. Rychkov. 2006. ClC-1 chloride channel: matching its properties to a role in skeletal muscle. *Clin. Exp. Pharmacol. Physiol.* 33:1118–1123. doi:10.1111/j.1440-1681.2006.04502.x

Ashcroft, F.M., J.A. Heiny, and J. Vergara. 1985. Inward rectification in the transverse tubular system of frog skeletal muscle studied with potentiometric dyes. *J. Physiol.* 359:269–291.

Barry, P.H., and R.H. Adrian. 1973. Slow conductance changes due to potassium depletion in the transverse tubules of frog muscle fibers during hyperpolarizing pulses. *J. Membr. Biol.* 14:243–292. doi:10.1007/BF01868081

Bennetts, B., M.W. Parker, and B.A. Cromer. 2007. Inhibition of skeletal muscle ClC-1 chloride channels by low intracellular pH and ATP. *J. Biol. Chem.* 282:32780–32791. doi:10.1074/jbc.M703259200

Bezanilla, F., J. Vergara, and R.E. Taylor. 1982. Voltage clamping of excitable embranes. *In* Methods of Experimental Physics. Academic Press, New York. 445–511.

Bretag, A.H. 1987. Muscle chloride channels. *Physiol. Rev.* 67:618–724.

Bryant, S.H., and A. Morales-Aguilera. 1971. Chloride conductance in normal and myotonic muscle fibres and the action of monocarboxylic aromatic acids. *J. Physiol.* 219:367–383.

Coonan, J.R., and G.D. Lamb. 1998. Effect of transverse-tubular chloride conductance on excitability in skinned skeletal muscle fibres of rat and toad. *J. Physiol.* 509:551–564. doi:10.1111/j.1469-7793.1998.551bn.x

Crank, J. 1975. The Mathematics of Diffusion. Second ed. Oxford University Press, Oxford, UK. 414 pp.

De Jongh, K.S., C. Warner, A.A. Colvin, and W.A. Catterall. 1991. Characterization of the two size forms of the alpha 1 subunit of skeletal muscle L-type calcium channels. *Proc. Natl. Acad. Sci. USA.* 88:10778–10782. doi:10.1073/pnas.88.23.10778

DiFranco, M., J. Capote, and J.L. Vergara. 2005. Optical imaging and functional characterization of the transverse tubular system of mammalian muscle fibers using the potentiometric indicator di-8-ANEPPS. *J. Membr. Biol.* 208:141–153. doi:10.1007/s00232-005-0825-9

DiFranco, M., J. Capote, M. Quinonez, and J.L. Vergara. 2007. Voltage-dependent dynamic FRET signals from the transverse tubules in mammalian skeletal muscle fibers. *J. Gen. Physiol.* 130:581–600. doi:10.1085/jgp.200709831

DiFranco, M., J. Capote, M. Quiñonez, and J.L. Vergara. 2008. Dynamic FRET signals between DPA and the α1s and β1a subunits of the DHPR of mammalian skeletal muscle fibers. *Biophys. J.* 94:880. doi:10.1016/S0006-3495(08)79157-4

DiFranco, M., M. Quinonez, J. Capote, and J. Vergara. 2009. DNA transfection of mammalian skeletal muscles using in vivo electroporation. *J. Vis. Exp.* 32:1520.

Dulhunty, A.F. 1979. Distribution of potassium and chloride permeability over the surface and T-tubule membranes of mammalian skeletal muscle. *J. Membr. Biol.* 45:293–310. doi:10.1007/BF01869290

Dulhunty, A. 1982. Effect of chloride withdrawal on the geometry of the T-tubules in amphibian and mammalian muscle. *J. Membr. Biol.* 67:81–90. doi:10.1007/BF01868650

Dutka, T.L., R.M. Murphy, D.G. Stephenson, and G.D. Lamb. 2008. Chloride conductance in the transverse tubular system of rat skeletal muscle fibres: importance in excitation-contraction coupling and fatigue. *J. Physiol.* 586:875–887. doi:10.1113/jphysiol.2007.144667

Eisenberg, R.S., and P.W. Gage. 1967. Frog skeletal muscle fibers: changes in electrical properties after disruption of transverse tubular system. *Science.* 158:1700–1701. doi:10.1126/science.158.3809.1700

Eisenberg, R.S., and P.W. Gage. 1969. Ionic conductances of the surface and transverse tubular membranes of frog sartorius fibers. *J. Gen. Physiol.* 53:279–297. doi:10.1085/jgp.53.3.279

Fahlke, C. 2001. Ion permeation and selectivity in ClC-type chloride channels. *Am. J. Physiol. Renal Physiol.* 280:F748–F757.

Fahlke, C., and R. Rudel. 1995. Chloride currents across the membrane of mammalian skeletal muscle fibres. *J. Physiol.* 484:355–368.

Fahlke, C., A. Rosenbohm, N. Mitrovic, A.L. George Jr., and R. Rudel. 1996. Mechanism of voltage-dependent gating in skeletal muscle chloride channels. *Biophys. J.* 71:695–706. doi:10.1016/S0006-3495(96)79269-X

Friedrich, O., T. Ehmer, D. Uttenweiler, M. Vogel, P.H. Barry, and R.H. Fink. 2001. Numerical analysis of Ca2+ depletion in the transverse tubular system of mammalian muscle. *Biophys. J.* 80:2046–2055. doi:10.1016/S0006-3495(01)76178-4

Gerald, C.F. 1978. Applied Numerical Analysis. Second ed. Addison-Wesley Publishing Company, Reading, MA. 518 pp.

Goldman, D.E. 1943. Potential, impedance, and rectification in membranes. *J. Gen. Physiol.* 27:37–60. doi:10.1085/jgp.27.1.37

Gurnett, C.A., S.D. Kahl, R.D. Anderson, and K.P. Campbell. 1995. Absence of the skeletal muscle sarcolemma chloride channel ClC-1 in myotonic mice. *J. Biol. Chem.* 270:9035–9038. doi:10.1074/jbc.270.16.9035

Heiny, J.A., and J. Vergara. 1982. Optical signals from surface and T system membranes in skeletal muscle fibers. Experiments with the potentiometric dye NK2367. *J. Gen. Physiol.* 80:203–230. doi:10.1085/jgp.80.2.203

Heiny, J.A., and J. Vergara. 1984. Dichroic behavior of the absorbance signals from dyes NK2367 and WW375 in skeletal muscle fibers. *J. Gen. Physiol.* 84:805–837. doi:10.1085/jgp.84.5.805

Heiny, J.A., F.M. Ashcroft, and J. Vergara. 1983. T-system optical signals associated with inward rectification in skeletal muscle. *Nature.* 301:164–166. doi:10.1038/301164a0

Herrera, A., M. DiFranco, and J.L. Vergara. 2010. An important fraction of the mammalian skeletal muscle chloride conductance is located in the transverse tubules. *Biophys. J.* 98:712a. doi:10.1016/j.bpj.2009.12.3906

Hodgkin, A.L., and P. Horowicz. 1959. The influence of potassium and chloride ions on the membrane potential of single muscle fibres. *J. Physiol.* 148:127–160.

Hodgkin, A.L., and P. Horowicz. 1960. The effect of sudden changes in ionic concentrations on the membrane potential of single muscle fibres. *J. Physiol.* 153:370–385.

Huser, J., P. Lipp, and E. Niggli. 1996. Confocal microscopic detection of potential-sensitive dyes used to reveal loss of voltage control during patch-clamp experiments. *Pflugers Arch.* 433:194–199. doi:10.1007/s004240050267

Jentsch, T.J., V. Stein, F. Weinreich, and A.A. Zdebik. 2002. Molecular structure and physiological function of chloride channels. *Physiol. Rev.* 82:503–568.

Kim, A.M., and J.L. Vergara. 1998a. Fast voltage gating of Ca2+ release in frog skeletal muscle revealed by supercharging pulses. *J. Physiol.* 511:509–518. doi:10.1111/j.1469-7793.1998.509bh.x

Kim, A.M., and J.L. Vergara. 1998b. Supercharging accelerates T-tubule membrane potential changes in voltage clamped frog skeletal muscle fibers. *Biophys. J.* 75:2098–2116. doi:10.1016/S0006-3495(98)77652-0

Klein, M.G. 1985. Properties of the chloride conductance associated with temperature acclimation in muscle fibres of green sunfish. *J. Exp. Biol.* 114:581–598.

Loew, L.M. 1993. Potentiometric Membrane Dyes. *In* Fluorescent and Luminescent Probes for Biological Activity. W.T. Mason, editor. Academic Press, London. 50–160.

Lueck, J.D., A. Mankodi, M.S. Swanson, C.A. Thornton, and R.T. Dirksen. 2007. Muscle chloride channel dysfunction in two mouse models of myotonic dystrophy. *J. Gen. Physiol.* 129:79–94. doi:10.1085/jgp.200609635

Palade, P.T., and R.L. Barchi. 1977. Characteristics of the chloride conductance in muscle fibers of the rat diaphragm. *J. Gen. Physiol.* 69:325–342. doi:10.1085/jgp.69.3.325

Papponen, H., T. Kaisto, V.V. Myllyla, R. Myllyla, and K. Metsikko. 2005. Regulated sarcolemmal localization of the muscle-specific ClC-1 chloride channel. *Exp. Neurol.* 191:163–173. doi:10.1016/j.expneurol.2004.07.018

Pusch, M. 2002. Myotonia caused by mutations in the muscle chloride channel gene CLCN1. *Hum. Mutat.* 19:423–434. doi:10.1002/humu.10063

Pusch, M., and T.J. Jentsch. 1994. Molecular physiology of voltage-gated chloride channels. *Physiol. Rev.* 74:813–827.

Pusch, M., K. Steinmeyer, M.C. Koch, and T.J. Jentsch. 1995. Mutations in dominant human myotonia congenita drastically alter the voltage dependence of the CIC-1 chloride channel. *Neuron.* 15:1455–1463. doi:10.1016/0896-6273(95)90023-3

Pusch, M., A. Liantonio, L. Bertorello, A. Accardi, A. De Luca, S. Pierno, V. Tortorella, and D.C. Camerino. 2000. Pharmacological characterization of chloride channels belonging to the ClC family by the use of chiral clofibric acid derivatives. *Mol. Pharmacol.* 58:498–507.

Rudel, R. 1990. The myotonic mouse–a realistic model for the study of human recessive generalized myotonia. *Trends Neurosci.* 13:1–3.

Rychkov, G.Y., M. Pusch, D.S. Astill, M.L. Roberts, T.J. Jentsch, and A.H. Bretag. 1996. Concentration and pH dependence of skeletal muscle chloride channel ClC-1. *J. Physiol.* 497:423–435.

Vergara, J., F. Bezanilla, and B.M. Salzberg. 1978. Nile blue fluorescence signals from cut single muscle fibers under voltage or current clamp conditions. *J. Gen. Physiol.* 72:775–800. doi:10.1085/jgp.72.6.775

Vergara, J.L., M. Delay, J.A. Heiny, and B. Ribalet. 1983. Optical studies of T-system potential and calcium release in skeletal muscle fibers. *In* The Physiology of Excitable Cells. A.D. Grenell and W.J. Moody, Jr., editors. Alan R. Liss, Inc., New York. 343–355.

Woods, C.E., D. Novo, M. DiFranco, and J.L. Vergara. 2004. The action potential-evoked sarcoplasmic reticulum calcium release is impaired in mdx mouse muscle fibres. *J. Physiol.* 557:59–75. doi:10.1113/jphysiol.2004.061291

Woods, C.E., D. Novo, M. DiFranco, J. Capote, and J.L. Vergara. 2005. Propagation in the transverse tubular system and voltage dependence of calcium release in normal and mdx mouse muscle fibres. *J. Physiol.* 568:867–880. doi:10.1113/jphysiol.2005.089318

Zhang, J., M.C. Sanguinetti, H. Kwiecinski, and L.J. Ptacek. 2000. Mechanism of inverted activation of ClC-1 channels caused by a novel myotonia congenita mutation. *J. Biol. Chem.* 275:2999–3005. doi:10.1074/jbc.275.4.2999

Zifarelli, G., and M. Pusch. 2008. The muscle chloride channel ClC-1 is not directly regulated by intracellular ATP. *J. Gen. Physiol.* 131:109–116. doi:10.1085/jgp.200709899